Correlations between D mesons and light hadrons in pp collisions at the ALICE experiment

– MASTER THESIS –

Eszter Frajna

Supervisor:
Róbert Vértesi
Senior Research Fellow
Department of High Energy Physics
Wigner Research Centre for Physics

Consultant:
Gábor Takács
Professor
Department of Theoretical Physics
BME

Budapest University of Technology and Economics
Faculty of Natural Sciences, Physics
2020

Önállósági nyilatkozat

Alulírott *Frajna Eszter* a Budapesti Műszaki és Gazdaságtudományi Egyetem fizika MSc szakos hallgatója kijelentem, hogy ezt a diplomamunkát meg nem engedett segédeszközök nélkül, önállóan, a témavezető irányításával készítettem, és csak a megadott forrásokat használtam fel. Minden olyan részt, melyet szó szerint, vagy azonos értelemben, de átfogalmazva más forrásból vettem, a forrás megadásával jelöltem.

Budapest, 2020. május 26.

.....

Aláírás

Research topic

The Large Hadron Collider (LHC) at CERN investigates the fundamental nature of the strong interaction in collisions of protons or heavy ions that are travelling at almost the speed of light. In these high-energy collisions, heavy (charm and bottom) quarks are created in the early stages of the reaction. Since they are produced in initial hard processes and their numbers are largely unchanged in the later stages of the reaction, they serve as ideal probes to test the validity of quantum colour dynamics as well as the properties of a strongly interacting hot and dense medium in a heavy ion collision. Launched in 2015, the LHC's Run-II phase, with the improved ALICE detector system, enabled the most precise heavy quark measurements ever. The candidate's task is to participate in the ALICE measurements of correlations between D-mesons and light hadrons in p–Pb collisions at 5 TeV, with simulation and methodological studies and possibly with data analysis. The results are essential to understand the fragmentation of heavy-flavour, as well as to gain a control over cold nuclear matter effects, thus setting the stage for the upcoming measurements in Pb-Pb collisions. While participating in the project, the candidate contributes to the operation and effectiveness of one of the world's leading experiments.

Contents

Chapter 1

Introduction

1.1 Ultra-relativistic heavy-ion physics

Our Universe was born about 13.7 billion years ago in a massive expansion called the Big Bang. The substance that is believed to have filled the Universe a few milliseconds after the explosion is called the Quark-Gluon Plasma (QGP). This state of matter exists at extremely high temperature and density. It consists of deconfined, strongly interacting quarks and gluons [1]. We can recreate the QGP in the laboratory in high-energy heavy-ion collisions.

The fundamental forces in the Universe are described by the Standard Model (SM) of the particle physics. The SM is a quantum field theory that involves all known elementary particles and the interactions among them. SM is based on symmetry principles, thus it is renormalizable and unitary. All predicted particles have been discovered experimentally and through many experiments, the Standard Model has become a well-tested theory.

There are twelve elementary particles of spin $\frac{1}{2}$, known as fermions (quarks and leptons), four particles with spin 1, known as bosons and one particle with zero spin, the so-called Higgs-boson. These particles are summarized in Figure 1.1.

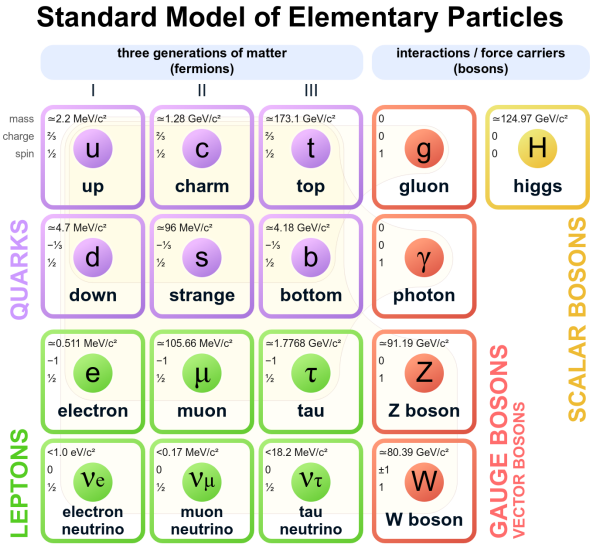

Figure 1.1: Standard Model of elementary particles.

Quarks are the only elementary particles to experience all four fundamental interactions (strong interaction, weak interaction, electromagnetism and gravity). There are six types of quarks, called flavours: up, down, strange, charm, bottom, and top. Up and down quarks have the lowest masses of all quarks (light quarks). The heavier quarks rapidly convert into up and down quarks through a process of weak particle decay: a flavour-changing transformation from a higher mass state to a lower mass state. Because of this, up and down quarks are the most common in the Universe, whereas strange, charm, bottom, and top quarks can only be produced in high-energy interactions. Quarks have fractional electric charge values depending on their flavour. Up, charm, and top quarks have a charge of +2/3, while down, strange, and bottom quarks have -1/3. For every quark flavour there is a corresponding type of antiparticle, known as an anti-quark, that differs from the quark only in that its electric charge has equal magnitude, but opposite sign.

Quarks have a quantum number called colour charge, which comes in 3 varieties: red, green and blue. In addition, each of them is complemented by an anticolour: antiblue, antigreen, and antired. A phenomenon known as colour confinement allows only states without colour charge. Although more exotic states may also exist, quarks usually compose colour neutral groups in two ways: a coloured quark and the corresponding anti-coloured quark form a pair (meson), or three different coloured quarks (blue, green, red) or three different anti-coloured quarks form a triplet (baryon or antibaryon). Mesons and baryons are called hadrons. Quarks are never found in isolation, therefore they cannot be observed directly.

The sector of the Standard Model that describes the strong interaction is called Quantum Chromodynamics (QCD). The strong force binds quarks together by the exchange of massless particles called gluons. Gluons carry a colour and an anticolour in 8 independent colour states. Unlike the electromagnetic force where electrically uncharged photons interact with charged particles, the gluons carry colour charge and can also interact with each other. As a result, the strong interaction between the two quarks does not decrease as the distance between the two quarks increases.

Even though, the Standard Model is currently the best description of particle physics, it does not give an answer to every question. Gravity is missing from the Model and several parameters must be set arbitrarily in it, such as the mass of neutrinos.

1.2 Basic concepts in particle collisions

In order to understand the physics of the collisions it is important to characterize the variables determining the particle movement in the detector.

The primary vertex is the interaction point of proton–proton (pp) collision. This can be measured by reconstructing the trajectory of the produced charged particles, since the orbits of the primary particles show back to this point.

In particle collisions, the size of the interaction area, and thus the area where Quark-Gluon Plasma is formed, is highly dependent on centrality (a quantity that expresses the extent of overlap between the colliding nuclei). Peripheral collisions are expected to be more similar to pp collisions than central collisions.

The energy in the Centre-of-Momentum Frame (COM frame) can be calculated using the four-vectors of the colliding beams, $E_\mu = (E, 0, 0, p_\mathrm{z})$, where E is the energy and p_z is the momentum

along the beam-pipe. If the particles has equal mass and energy, it is simply:

$$E_{\mathrm{COM}} = \sqrt{(E^{\mu} + E^{\vartheta})^2} = \sqrt{(2E)^2} = 2E, \tag{1.1}$$

i.e. twice the beam energy. The parameter s is a so-called Mandelstam variable, which is Lorentz invariant in general and $\sqrt{s}$ corresponds to the energy in the COM frame in pp collisions. When colliding particles consisting of more than one hadron, the energy per nucleon pair is denoted as $\sqrt{s_{\mathrm{NN}}}$. Using the available energy per nucleon pair makes it easier to compare heavy-ion experiments with different kinds of nuclei and pp collisions.

The three-momenta that describe the particles are often subdivided into two components according to the cylindrical symmetry around the beam axis: the longitudinal component $p_{\mathrm{L}} = p_{\mathrm{z}}$, parallel to the beam axis, and the transverse momentum component p_{T}:

$$p_{\mathrm{T}} = \sqrt{p_{\mathrm{x}}^2 + p_{\mathrm{y}}^2}. \tag{1.2}$$

The transverse momentum represents the momentum transfer that a produced particle gained during the interaction.

The azimuthal angle $\varphi = p_{\mathrm{y}}/p_{\mathrm{x}}$ of the particle is the angle in the x-y plane, perpendicular to the beam axis. The inclination measured relative to the beam direction in the z-y plane is characterized by the polar angle. Instead of the polar angle, it is worth introducing the rapidity defined as

$$y = \frac{1}{2}\ln\frac{E + p_{\mathrm{z}}}{E - p_{\mathrm{z}}}, \tag{1.3}$$

which is additive to Lorentz transformation. In the approximation where the particle is traveling close the speed of light, or equivalently in the limit where the particle mass is negligible compared to the momentum, the definition of rapidity converges to the so-called pseudorapidity:

$$\eta = \frac{1}{2}\ln\frac{p + p_{\mathrm{z}}}{p - p_{\mathrm{z}}} = -\ln(\tanh(\vartheta/2)). \tag{1.4}$$

The motion of particles in the detector is determined by the pseudorapidity (η) and the azimuthal angle (φ).

In relativistic hydrodynamical descriptions it is also useful to introduce the transverse kinetic energy (KE_{T}):

$$KE_{\mathrm{T}} = m_{\mathrm{T}} - m, \tag{1.5}$$

where $m_{\mathrm{T}} = \sqrt{m^2 + p_{\mathrm{T}}^2}$ and m is the particle mass.

1.3 The strongly interacting Quark-Gluon Plasma

High-energy collisions of heavy quarks provide the opportunity to recreate the QGP for a short moment in laboratory experiments and study its properties. Scattering processes in such collisions can be classified as either soft or hard, based on the magnitude of the transmitted momentum. Hard processes are common in the early stages of a collision. In these processes few particles are involved, typically with high momenta. Such processes can be theoretically calculated using per-

turbative quantum field theory. In case of the presence of the Quark-Gluon Plasma, these particles can be used as self-generated tomographic probes that can detect any nuclear modification by the QGP, compared to the vacuum case. In contrast, soft processes come from later stages in which many particles with low momentum are involved. Soft probes of the Quark-Gluon Plasma are, for example, measurements of global characteristics and collectivity.

1.3.1 Discovery of the Quark-Gluon Plasma

In a very simple approximation called the string model of quarks, the potential between quarks can be written as approximately $U{=}\sigma r$, where colour field lines are organized similarly to a flexible string [2]. When two quarks move away from each other with high momentum, more and more energy is accumulated in colour confinement due to the interaction of the gluons. Therefore, as two colour charges are separated, at some point it becomes energetically favorable for a new quark–antiquark pair to appear, rather than extending the tube further. Quarks are transformed into hadrons until only bound states can be observed. The process in which a parton (a high-momentum quark or gluon) breaks into multiple hadrons is called fragmentation, and the collimated shower of particles created by the fragmentation of a single parton is called a jet. Jets are measured and studied in particle detectors to determine the properties of the original partons [3]. Jets can also be used in hard tomographic probes to understand the properties of the Quark-Gluon Plasma via their modification.

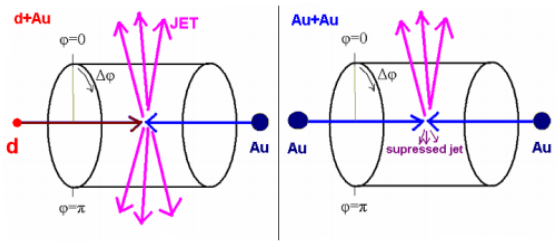

Figure 1.2: Schematic drawing of the phenomenon of jet supression in central heavy ion collisions. The left-side cartoon shows a d–Au collision, where the two jets leave the detector because of the absence of the hot medium. In the right-side cartoon, in the Au–Au collision, the coloured medium absorbs one of the jets.

In the Relativistic Heavy Ion Collider (RHIC), proton–proton (pp), deuteron–gold (d–Au) nuclei and gold–gold (Au–Au) nuclei collisions were studied. Figure 1.2 schematically illustrates the collisions of heavy ions in the detector. Jets can be observed in each type of the collisions. Since jets stem from high-momentum partons, they are mostly produced as back-to-back pairs. A collision is called central if the nucleus that collide onto each other overlap to a large extent.

It has been predicted that in central Au–Au collisions in the case of a large transverse momentum ($p_{\mathrm{T}} > 2$ GeV/c) jets that penetrate the medium are quenched and they lose a large part of their momentum [4]. Figure 1.3 shows the two-particle azimuthal correlation data of STAR, in which the phenomenon of jet quenching can be observed. In the case of small angular differences at the near-side peak ($\Delta\phi \approx 0$) a similar correlation peak can be observed in pp, d–Au and Au–Au collisions. However, at the central Au–Au collisions at the away-side peak ($\Delta\phi \approx \pi$) is completely attenuated, while it is present in pp collisions. This suggests that if one of the jets is has to pass

through a medium, it loses its energy. We also do not experience jet quenching in the case of a d–Au collision, despite the fact that there is nuclear material there, albeit hadronic (cold). This demonstrates that jet quenching originates from the final state of central heavy-ion collisions, via the interaction with the hot and dense nuclear matter. In peripheral collisions, when the overlap of the nuclei is much smaller, this effect practically disappears, the two peaks are similar to the pp and d–Au collisions [5, 6, 7, 8].

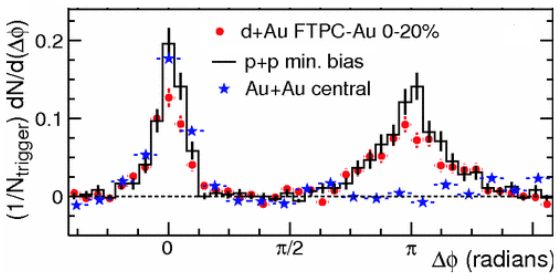

Figure 1.3: Azimuthal correlations of high-momentum particles in the STAR measurement, which clearly showing the phenomenon of jet suppression at central Au–Au collisions, as the complete absence of the correlation peak $\Delta\phi = \pi$ [9].

This result confirms that high-density strongy interacting material is created in Au–Au collisions that cannot be made up of hadrons, but instead it has to undergo a phase transition into a state where the components of the hadrons are free and form a hot, strongly interacting medium that suppresses the jets. Experiments demonstrating jet quenching at RHIC provided the first convincing evidence for the existence of the Quark-Gluon Plasma.

1.3.2 Exploring the properties of the QGP and the QCD phase diagram

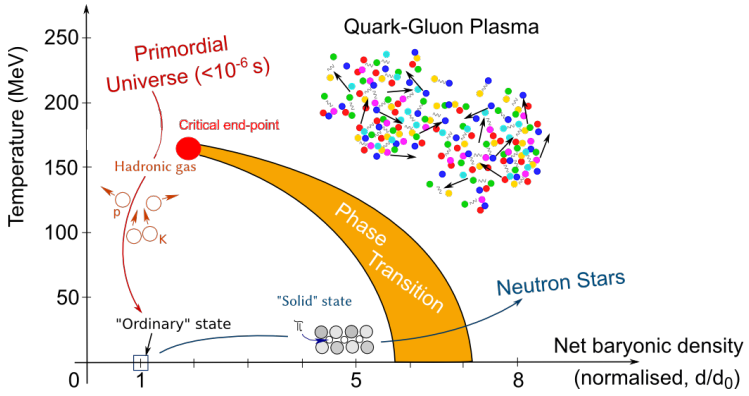

Figure 1.4: Schematic view of the phase diagram of strongly interacting matter, in terms of the baryonic density and the temperature [12].

High-energy collisions of heavy ions provide the opportunity to recreate the QGP for a short moment in laboratory experiments and study its properties [10]. Experiments at RHIC have revealed that the Quark-Gluon Plasma created in the colliders does not behave as an asymptotically free ideal gas, but as a strongly coupled, almost perfect liquid [5, 6, 7, 8]. Figure 1.4 shows an illustration of the QCD phase diagram. At low baryon density and low temperature, the QCD matter

exists in the form of hadron gas in which the quarks and gluons are confined inside hadrons. With an increase of temperature and density, the nuclear matter will transition into a colour-deconfined Quark-Gluon Plasma state. The orange band is a schematic boundary between the different phases as expected from theoretical model calculations. Based on lattice-QCD calculations [11] this is a first-order phase transition for a high net baryon density with a critical end-point, and a continuous transition for a lower net baryon density. Experiments at facilities such as RHIC and the LHC probe the phase transition from deconfined to confined matter at different baryon densities.

The Quark-Gluon Plasma behaves as a strongly coupled fluid that can be well described by viscosity-free hydrodynamic models [8]. The initial geometry of the collisions cannot be measured directly, however, final-state distributions can be measured. The spatial anisotropy initially present in non-central collisions is transformed into momentum space anisotropy during collective expansion. The various patterns of anisotropic flow are characterized by the Fourier expansion of the invariant triple differential distributions:

$$E\frac{\mathrm{d}^3N}{\mathrm{d}^3\mathbf{p}} = \frac{1}{2\pi}\frac{\mathrm{d}^2N}{p_\mathrm{T}\mathrm{d}p_\mathrm{T}\mathrm{d}y}\left(1+2\sum_{n=1}^{\infty}v_n\cos[n(\varphi-\phi_\mathrm{RP})]\right), \tag{1.6}$$

where E is the energy of the particle, N is the number of formed particles, $\mathbf{p}$ is the three-momentum vector, p_t is the transverse momentum, φ is the azimuthal angle, y is the rapidity and ϕ_RP is the reaction plane angle [13]. The Fourier coefficients are given by:

$$v_n(p_\mathrm{T}, y) = \langle\cos[n(\varphi-\phi_\mathrm{RP})]\rangle, \tag{1.7}$$

where the angular brackets denote an average over the particles, summed over all events. In this Fourier decomposition, the coefficients v_1 and v_2 are known as directed flow and elliptic flow, respectively.

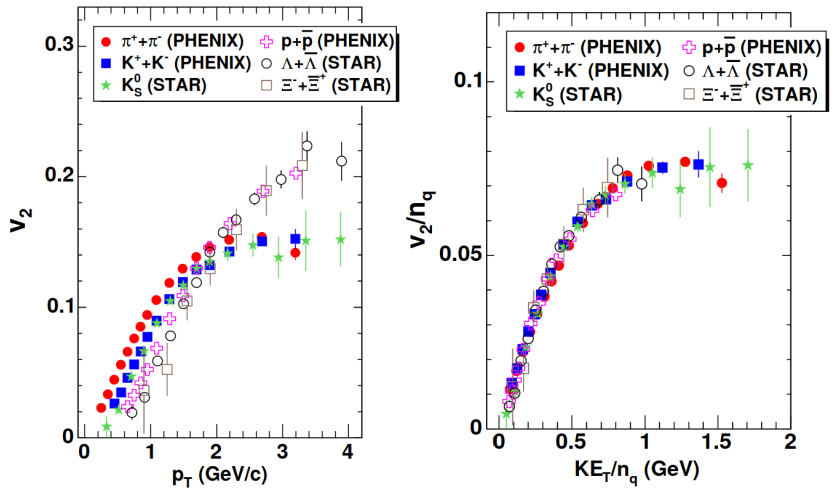

Figure 1.5: The v_2 as a function of p_T (right) and v_2/n_q as a function of $KE_\mathrm{T}/n_\mathrm{q}$ in Au–Au collisions [14].

Figure 1.5 shows a comparison of the different particle species' differential anisotropy (v_2) as a function of p_T and the transverse kinetic energy (KE_T) in Au–Au collisions. As demonstrated

in the figure, a substantial v_2 is present in non-central heavy-ion collisions. This is only expected in the strongly coupled case where the initial spatial anisotropy transforms into momentum space anisotropy during collective expansion. If an non-interacting or only weakly interacting hadron gas was formed in heavy ion collisions, one would not see such pattern. If one scales the v_2 with the number of constituent quarks of each hadron species and plots it against the transverse kinetic energy KE_{T}, an almost perfect scaling behavior appears. This indicates that the fundamental degrees of freedom during the development of collectivity are provided by the quarks.

1.4 Heavy-flavour measurements in high-energy collisions

The c ($m_c = 1.27$ GeV/c^2), b ($m_b = 4.2$ GeV/c^2), and t ($m_b = 173$ GeV/c^2)quarks are called heavy quarks, because of their large mass compared to the other quarks. All conventional matter is made up of two light quarks: up ($m_u = 2.3$ MeV/c^2) and down ($m_d = 4.8$ MeV/c^2) quarks. Heavy quarks can be found in unstable hadrons that are difficult to create and decay quickly. However, heavy-flavour quarks are an excellent tool to study heavy-ion collisions. Most of them are created in the initial stages of the reaction, which means that their formation is not affected by the medium. It allows the use of analytical (perturbative) quantum colour dynamics calculations. Zweig's rule states that the more annihilation steps a final state develops, the less likely it is to occur, thus the heavy-quark annihilation cross section is negligible. Based on their spatial and momentum distributions, we can trace back the interactions of heavy quarks with the medium. From the three heavy quarks, c-quarks and b-quarks are used to study heavy ion collisions. This is due to the fact that their long lifetime ensures that they interact both with the hot and dense medium as well as with the cold hadronic matter before they decay.

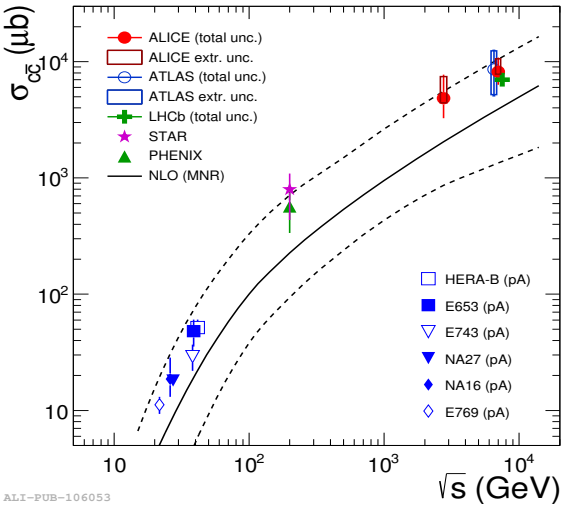

Figure 1.6: Total inclusive charm production cross section in nucleus–nucleus collisions as a function of $\sqrt{s}$ [15].

Heavy quarks (c, b) hadronize into mesons (D, B) or baryons. These hadrons later decay weakly into light mesons. In the experiment we can reconstruct the properties of heavy hadrons from the kinematic properties of these decay products. By comparing the yields of light and heavy

quarks, we can understand the dependence of the formation and hadronization processes of the partons (quarks or gluons) and their interaction with the medium on the colour charge and the parton mass. The participation of heavy quarks in the collective motion carries information about the thermal behavior of the Quark-Gluon Plasma [16, 17].

According to our current knowledge, no Quark-Gluon Plasma is formed in pp collisions. Thus, on the one hand, these collisions serve as a primary test for vacuum quantum color dynamics models, and on the other hand, they can be used as a reference for understanding nuclear material modifications in p–A and A–A collisions. The differential production cross section of heavy quarks was determined by ALICE in high-precision measurements in several channels, which one can see in Figure 1.6, including the the direct reconstruction of D mesons containing c quarks and B mesons containing b quarks, and the measurement of the spectrum of electrons and muons [18, 19] from the semileptonic decay channels of heavy mesons. In general, models based on perturbative QCD describe measured data well, however, the scale uncertainty of these models is much higher than the measurement accuracy available today. Therefore, experiments are increasingly turning to rarer, more detailed, more differential probes to constrain models through multiple observables.

Identifying characteristic correlation patterns of heavy and light quarks can help understand flavour-dependent fragmentation. Furthermore, finding these characteristic shapes can be used as an alternative method to pin down feed-down of beauty hadrons into charm without the need to find the location where the hadrons containing heavy quarks decay to light hadrons (secondary vertex) [20]. While measuring the yield of heavy quarks provides insight into the perturbatively computable processes of flavour-dependent parton formation, the study of the jet structures also provides information on fragmentation processes that cannot be calculated analytically. The azimuthal correlation of D mesons with light charged hadrons reveals information of the formation of the jet structure. The ALICE collaboration performed measurements of D meson and hadron (D–h) correlations in pp and p–Pb collisions with $\sqrt{s}$ = 5.02 TeV energy [21]. The obtained results can be well described by detailed simulation of collision events and modeling of the detector response, and it can be used to separate the components of the final correlation image from the different steps of the reaction [20, 22]. The correlation peaks correspond to the two-jet events formed in the initial processes, and later parton radiations and multi-parton interactions contribute in different ways. In this thesis I summarize my work directed to the exploration of these effects.

1.5 Collectivity in small, strongly interacting systems

The traditional assumption is that the energy density in collisions of small systems (such as pp and p–Pb) is not high enough for the formation of QGP. However, early LHC measurements already showed that there are long-range multiparticle correlations [23, 24] similar to those that are present in heavy-ion collisions. But it still has to be understood whether the similarities of high multiplicity p–Pb (and maybe pp) collisions and heavy ion collisions originate from the same mechanisms [25].

In order to characterize azimuthal correlations in small systems over a broad kinematic range, it is important to take into account the initial-state and final-state effects. Figure 1.7 shows a schematic illustration of the long range azimuthal correlation strength as a function of the event multiplicity (the number of he particles in the events) in small systems. In low-multiplicity events

the azimuthal correlations are primarily due to back-to-back minijets. Minijets are semi-hard partons produced in a collision of multiple incoming partons (also called multiple-parton interactions), or in a bremsstrahlung process [26]. When increasing the multiplicities, final-state interactions can no longer be neglected and this lead to a depletion of initial-state correlations. The system starts to demonstrate a response to the initial-state geometry. At high-multiplicity mostly the hydrodynamic expansion of a Quark-Gluon Plasma influence azimuthal correlations.

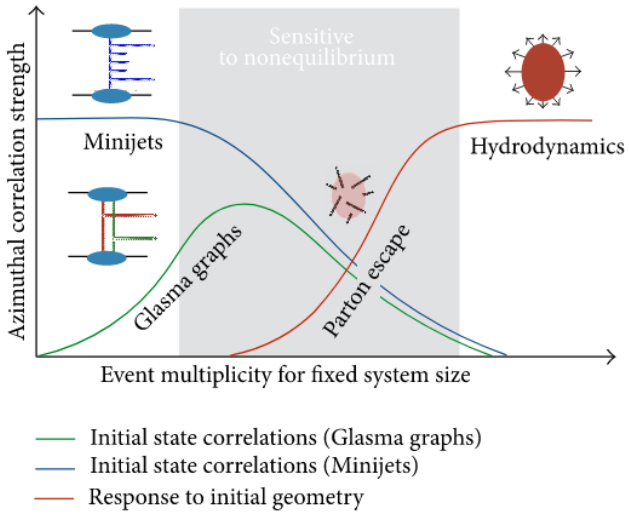

Figure 1.7: Illustration of long range azimuthal correlations in small systems [27].

Multiplicity-dependent probes with light and heavy flavors can help us to experimentally disentangle these effects and pin down the origin of collective features from small to large systems. In the current work I examine the role of QCD effects from the soft-hard boundary in the development of D–h correlation patterns. A natural continuation of the studies detailed in this work is to observe D–h correlations in high-multiplicity events.

Chapter 2

Experimental methods

2.1 The LHC and the ALICE detector

The Large Hadron Collider (LHC) is located near Geneva, Switzerland, built by the European Organization for Nuclear Research (CERN). The LHC is a 27-kilometer-circumference synchrotron ring that can accelerate protons or heavy ions to near the speed of light through a changing electric field. The beam of charged particles is held in orbit and focused by superconducting magnets.

Four large detectors have been constructed at the LHC, which are designed to investigate hadron–hadron collisions. ATLAS and CMS focus on pp collisions, in particular to measure the Higgs boson properties and to better understand the Standard Model, as well as to explain physics beyond the Standard Model. LHCb focuses primarily on measuring b-quarks in pp collisions, its main purpose is to accurately understand the electro-weak sector (e.g., accurate measurement of CP violation). ALICE (A Large Ion Collider Experiment) is specifically optimized to study heavy-ion collisions (mainly Pb–Pb), but taking data from pp collisions is equally part of the program, especially to compare data with heavy ions [28, 29]. Data is then moved to the Worldwide LHC Computing Grid, where it is processed, stored and analyzed [30].

Since in today's large experiments it is impossible to record all the data from every collision, a trigger system is used to select collisions that contain interesting physics, based on specific criteria. In order to interpret and study particle interactions in ALICE, we need to reconstruct the tracks of particles coming from the reaction.

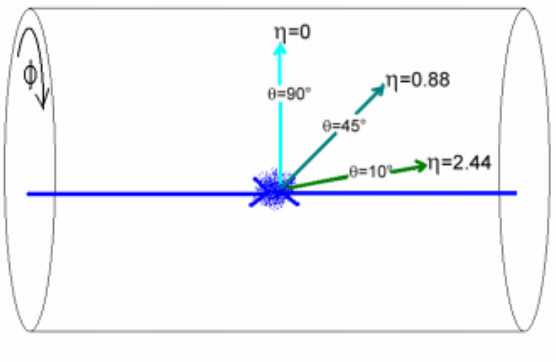

Figure 2.1: Sketch of the ALICE coordinate system.

A sketch of the ALICE coordinate system is shown in Figure 2.1. It is a right-handed orthogonal Cartesian system. The x axis is perpendicular to the mean beam direction, aligned with the local horizontal and pointing to the accelerator centre. The y-axis is perpendicular to the x axis and the beam direction and pointing upward. The x-y plane is called the transverse plane. The beam direction (z) is called the longitudinal direction. The motion of particles in the detector is determined by the pseudorapidity (η) and the azimuthal angle (φ). The azimuthal angle is measured in the x-y plane from the x-axis.

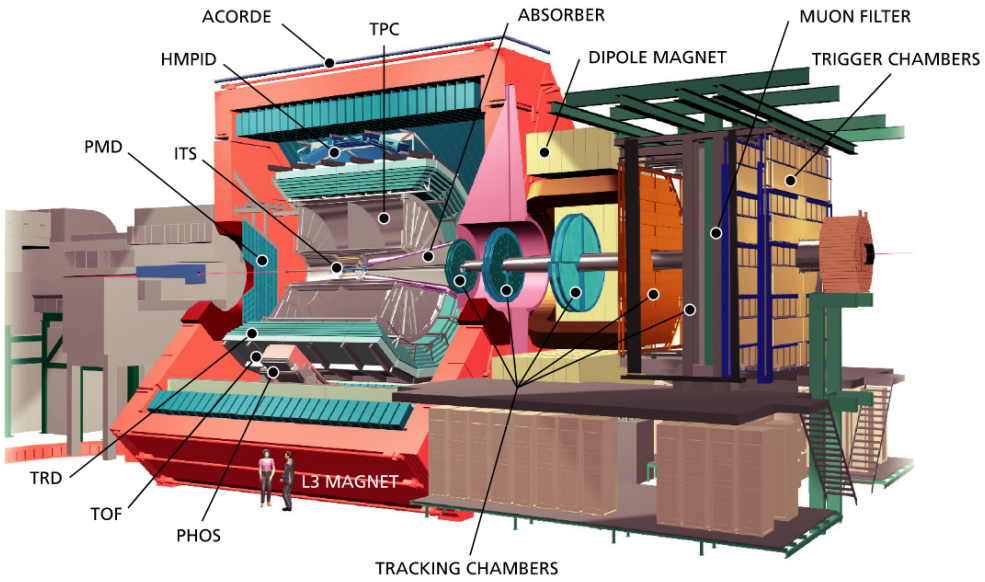

Figure 2.2: An illustration of the ALICE detector with all the subdetectors indicated.

ALICE is using a set of 18 subdetectors in order to identify all the particles that are coming out of the system as one can see in Figure 2.2. They give information about the mass, the velocity and the electrical charge of the particles. The main tracking device is the Time Projection Chamber (TPC) designed to track and identify the thousands of particles created in each collision. The Inner Tracking System (ITS) close to the interaction point determines the secondary vertex position, tracks particles and contributes to triggering. The Electro-Magnetic Calorimeter (EMCal) measures the energy of particles, to identify these particles and determine whether they have electromagnetic or hadronic interactions. The kinematics of unstable particles are reconstructed based on their invariant mass distributions from their decay products. Finally, we need to know how central the collision was, that is, to what extent did the colliding nuclei overlap. This is done by measuring the remnants of the colliding nuclei in the Zero Degree Calorimeter and by measuring the number of particles produced in the collision and their spatial distribution with V0 and T0 detectors. A detailed description of the detector is presented in Ref. [31].

The ALICE experiment allows us to observe the phenomenon of phase transition, identify missing segments in the phase diagram of a nuclear material, search for additional properties of quantum colour dynamics and strong interaction, analyze the fine structure of a vacuum, and examine how the material behaved immediately after the Big Bang.

2.2 Correlation methods

Two-particle angular correlations are an excellent tool to investigate the mechanisms of particle production and study the event properties of ultra-relativistic hadronic collisions. They are especially effective in the p_{T} ranges ($p_{\mathrm{T}} \sim$ 1–3 GeV/c) on the soft-hard boundary where jet-medium interactions and semi-hard QCD processes are present, and a full jet reconstruction may be problematic [32]. In fact, one of the first proofs of the QGP was by correlation measurements, as described in Sec. (1.3.1).

The p_{T} dependence of the correlation is studied by measuring triggered correlations. In such an analysis, a particle is chosen from a p_{T} region and called the trigger particle. The so-called associated particles from another p_{T} region are correlated to the trigger particle where $p_{\mathrm{T}}^{\mathrm{assoc.}} < p_{\mathrm{T}}^{\mathrm{trig.}}$. The associated per-trigger yield is measured as a function of the azimuthal angle difference $\Delta\varphi = \varphi_{\mathrm{trig.}} - \varphi_{\mathrm{assoc.}}$ and pseudorapidity difference $\Delta\eta = \eta_{\mathrm{trig.}} - \eta_{\mathrm{assoc.}}$:

$$Y(\Delta\varphi, \Delta\eta) = \frac{1}{N_{\mathrm{trig.}}} \frac{\mathrm{d}^2 N_{\mathrm{assoc.}}}{\mathrm{d}\Delta\varphi \mathrm{d}\Delta\eta}, \tag{2.1}$$

where $N_{\mathrm{assoc.}}$ is the number of particles associated to a number of trigger particles, $N_{\mathrm{trig.}}$. This quantity is measured for different ranges of $N_{\mathrm{trig.}}$ and $N_{\mathrm{assoc.}}$ within each event. The plane $(\Delta\varphi, \Delta\eta)$ can be divided into two parts along $\Delta\varphi$: the near-side and away-side peak regions. The near-side peak defined as the range from $-\frac{\pi}{2}$ to $\frac{\pi}{2}$, and the away-side as the range from $\frac{\pi}{2}$ to $-\frac{3\pi}{2}$. Near-side correlations give information about the structure of jets since, after background subtraction, most trigger and associated particles come from the same jet. Differences between correlations of beauty, charm and light flavour provide valuable information about flavour-dependent jet fragmentation. Away-side correlation is mostly from back-to-back jet pairs and it is sensitive to the underlying hard processes.

The azimuthal and pseudorapidity distribution of associated, charged particles with respect to a trigger, D meson is sensitive to the charm-quark production, fragmentation, and hadronisation processes in proton-proton (pp) collisions and to their possible modifications in larger collision systems, like proton-nucleus or nucleus-nucleus. In my thesis, I examine two-particle correlations in more detail.

2.3 Simulation of high-energy collisions with PYTHIA 8

In the LHC, jets coming from the final state are reconstructed from their particle track momenta. The measurements can be compared to predictions from parton shower Monte Carlo simulations. Simulations are used in many fields of high-energy physics, such as modeling the detector response, estimating background processes, determining selection efficiency and sample purity, and preliminary estimation of the magnitude of a given experimental signal. Therefore, it is important to use simulations that describe well the elementary processes.

PYTHIA 8 [22] is a Monte Carlo based event generator for simulating high-energy physics events. In the studies presented in this thesis I used PYTHIA 8, which is one of the most versatile and widely-used software packages in high-energy physics. It includes the initial-state develop-

ment, multiple interactions and the final-state interactions, as illustrated in Figure 2.3. It allows for the generation of ultra-relativistic collisions of leptons and/or hadrons. It employs $2 \to 2$ QCD matrix elements evaluated perturbatively with leading-order precision (LO), with the next-to-leading order (NLO) contributions taken into account during the parton showering stage.

The principal challenge when trying to make theoretical predictions or interpret experimentally detected final states is that the theory of the strong interactions (QCD) is most simply applied to the short distance degrees of freedom (the colour-charged quarks and gluons). At large momentum or at short distances, the QCD is asymptotically free, which implies that the coupling constant is small, so one can apply the non-perturbative physics. While in the detectors we observe colour singlet bound states (long distance degrees of freedom). The hard scattering event occurs in many different steps.

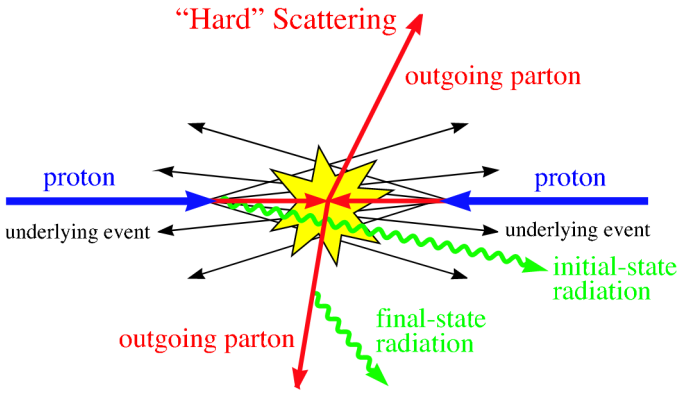

Figure 2.3: An illustration of a hard scattering event [33].

The first step is selection of the incident beam particles from the partons that participate in the short distance scattering. Before the short distance scattering these partons can emit radiation which is called initial state radiation (ISR). Since hadrons are composite objects, more than one distinct hard parton interactions can occur, and remnants can also rescatter on each other. These processes are called the multiple parton interactions (MPI). Examples of MPI can be seen in Figure 2.4. MPI is responsible for the production of much of the soft partons, or the underlying event (UE). In PYTHIA, MPI is implemented interleaved with ISR processes.

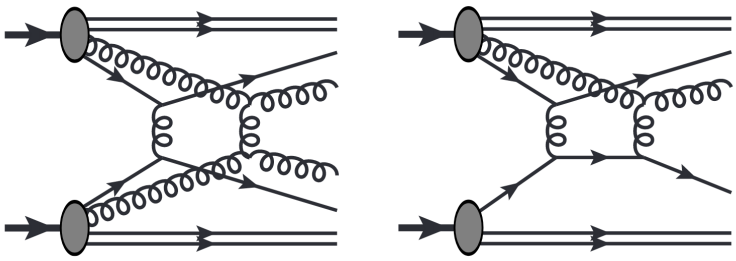

Figure 2.4: Illustration of multiple parton interactions. Two $2 \to 2$ scatterings (on the **right** side) and a $2 \to 2$ scattering followed by a rescattering (on the **left** side) [34].

Colour reconnection is a built-in mechanism in PYTHIA that allows interactions between par-

tons originating in multiple parton interactions (MPI) and initial/final state radiations (ISR/FSR), by minimizing colour string length, as illustrated in Figure 2.5. Colour reconnection is handled based on phenomenological models, and there are multiple approaches.

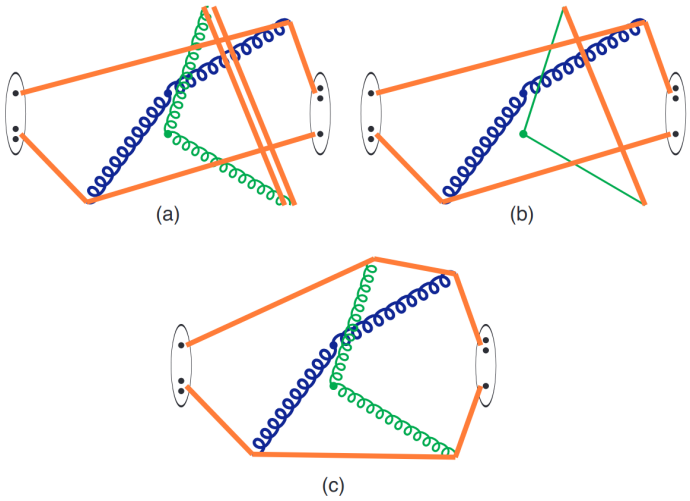

Figure 2.5: Illustration of colour reconnection. Thick blue lines denote outgoing gluons from the primary interaction, thin green lines of gluons or quarks denote the partons of a further MPI, black ovals denote the beam remnants with valence quarks, and orange thick lines denote the colour strings stretched between the partons [35].

Next comes the short distance scattering process that can produce more partons. Then comes another colour radiation step, with many new gluons and quark pairs. This is called final state radiation (FSR). This step is dominated by partons that have low energy and is nearly collinear with the scattered short distance partons. The FSR and the ISR are described in the Monte Carlo programs and calculated with leading logarithm perturbation theory.

The final step involves a non-perturbative hadronization process that organizes the coloured degrees of freedom into colour-singlet hadrons with physical masses. The details are determined from measurement data but the decay modes are not well-understood leading to uncertainties and differences between Monte Carlo programs in the details of the production of the final state hadrons.

The PYTHIA 8 Monte Carlo generator integrates all these components (or a selected subset of them) in a consistent set of physical models. It is capable of producing a multiparticle final state after hard scattering of a few particles.

Chapter 3

Phenomenological studies of heavy-flavour correlations

3.1 Analysis method

I investigated the angular correlations of heavy and light flavors in simulations at LHC energies at mid-rapidity. The following simulation results serve as a case study that the techniques I developed can be successfully applied in today's large experiments such as ALICE at the LHC to aid and interpret heavy-flavor correlation measurements.

I used the PYTHIA 8.1 Monte Carlo event generator [22] to simulate hard QCD events using the default Monash 2013 [36] tunes for LHC pp data. Five million pp collision events were simulated at a time, at the center-of-mass energy of $\sqrt{s} = 7$ TeV. The phase space has been reduced so that the leading hard process has minimum transverse momentum of $\hat{p}_{\mathrm{T}} = 5$ GeV/c. Heavy flavour scale settings were used similarly to recent STAR analyses, e.g., that in [37]. For beauty and charm simulations, only the two-to-two processes were enabled ($gg \to b\bar{b}$ and $qq \to b\bar{b}$, as well as $gg \to c\bar{c}$ and $qq \to c\bar{c}$, respectively), while light hadron correlations were simulated by allowing all hard quantum colour dynamics processes.

To examine the correlation of particles, I followed a technique similar to [32], as detailed in Section 2.2. I selected a trigger particle from a given momentum (p_{T}) range, and associated particles from a lower momentum (p_{T}) window to examine all other particles from the same event. Then I calculated the differences in the azimuth angles as well as the pseudorapidities of the trigger and associated particles within each event. The plane ($\Delta\eta, \Delta\varphi$) can be divided into two parts along $\Delta\varphi$: near-side and away-side peak region. I defined near-side as the range from $-\pi/2$ to $\pi/2$, and the away-side as the range from $\pi/2$ to $3\pi/2$.

I examined the width of fitted functions in the $5 < p_{\mathrm{T}}^{trigger} < 8$ GeV/c trigger particle transverse momentum range, and in different associated particle transverse momentum ($p_{\mathrm{T}}^{assoc.}$) ranges ($1 < p_{\mathrm{T}}^{assoc.} < 2$ GeV/c, $2 < p_{\mathrm{T}}^{assoc.} < 3$ GeV/c, $3 < p_{\mathrm{T}}^{assoc.} < 5$ GeV/c and $5 < p_{\mathrm{T}}^{assoc.} < 8$ GeV/c). In the latter case I ensured that $p_{\mathrm{T}}^{trigger} > p_{\mathrm{T}}^{assoc.}$.

Correlation analyses usually use the mixed-event technique to correct for the finite size of the detector in η [32]. However, at mid-rapidity it is sufficient to assume a uniform track distribution

and therefore I apply a reweighting of events with a "tent-shaped" function:

$$\frac{\mathrm{d}N}{\mathrm{d}\Delta\eta} = \frac{1}{2A} - \frac{|\eta|}{4A^2}, \tag{3.1}$$

where $A = 2$ is the maximal acceptance in which tracks were recorded. In the analysis, I only used the $|\Delta\eta| < 1.6$ range. On the right side of Figure 3.1, one can see the acceptance correction and on the left side the correlation peak after the acceptance correction.

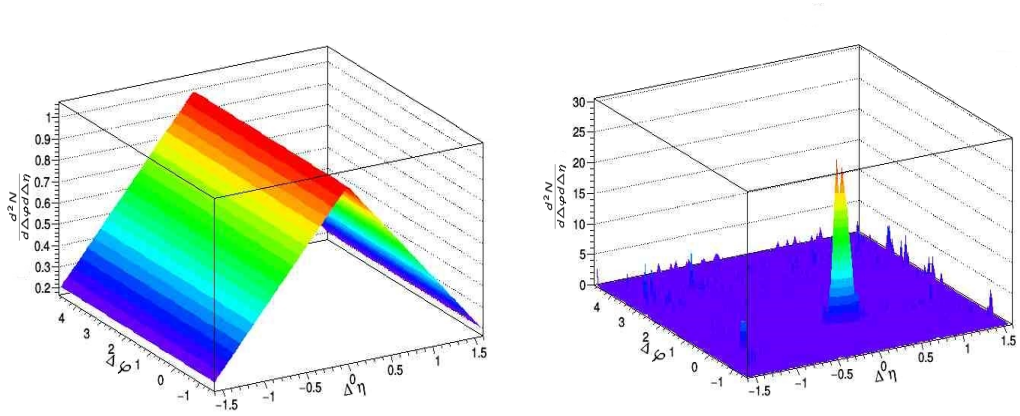

Figure 3.1: The acceptance correction (on the **right** side) and the correlation peak after the acceptance correction (on the **left** side).

Processes that fulfilled the conditions of the central limit theorem yield Gaussian-shaped correlation peaks. In case of weakly decaying resonances corresponding to secondary vertices that can be displaced with several millimeters, however, the Gaussian shape is not necessarily adequate. Therefore I also apply a generalised Gaussian fit on the near- and away-side correlation peaks. Gaussian functions of the different projections are

$$f(\Delta\varphi) = N \cdot \frac{1}{\sqrt{2\pi}\sigma_{\Delta\varphi}} \cdot e^{-\left(\frac{\Delta\varphi^2}{2\sigma^2_{\Delta\varphi}}\right)}, \quad f(\Delta\eta) = N \cdot \frac{1}{\sqrt{2\pi}\sigma_{\Delta\eta}} \cdot e^{-\left(\frac{\Delta\eta^2}{2\sigma^2_{\Delta\eta}}\right)}, \tag{3.2}$$

and the generalised Gaussian functions of the different projections are

$$g(\Delta\varphi) = N \cdot \frac{\gamma_{\Delta\varphi}}{2\omega_{\Delta\varphi}\Gamma\left(\frac{1}{\gamma_{\Delta\varphi}}\right)} \cdot e^{-\left(\frac{|\Delta\varphi|}{\omega_{\Delta\varphi}}\right)^{\gamma_{\Delta\varphi}}}, \quad g(\Delta\eta) = N \cdot \frac{\gamma_{\Delta\eta}}{2\omega_{\Delta\eta}\Gamma\left(\frac{1}{\gamma_{\Delta\eta}}\right)} \cdot e^{-\left(\frac{|\Delta\eta|}{\omega_{\Delta\eta}}\right)^{\gamma_{\Delta\eta}}}, \tag{3.3}$$

where N is the normalization factor, $\Gamma(z) = \int_0^\infty x^{z-1}e^{-x}\mathrm{d}x$ is the gamma function, $\sigma_{\Delta\varphi}$ is the width of the peak in the direction of $\Delta\varphi$, and $\sigma_{\Delta\eta}$ is the width of the peak in the direction of $\Delta\eta$. The generalised Gaussian function has an extra parameter γ compared to the Gaussian. If $\gamma = 1$, then the generalised Gaussian function is an exponential function. If $\gamma = 2$, it is reduced to a regular Gaussian function. If γ is greater than two then the top of the function is flattened.

3.2 Results

3.2.1 Correlations of light charged hadrons

As a first test I reproduced the near- and away-side correlation peaks of light charged hadrons ($\pi^{\pm}$, $K^{\pm}$, p and $\bar{p}$) both in the $\Delta\eta$ and the $\Delta\varphi$ directions. For all the particles I investigated in this study, I only examined the near-side peak in the direction of $\Delta\eta$, and in the direction of $\Delta\varphi$ I investigated both peaks. Below, the parameters are shown in different $p_{\mathrm{T}}^{assoc.}$ ranges.

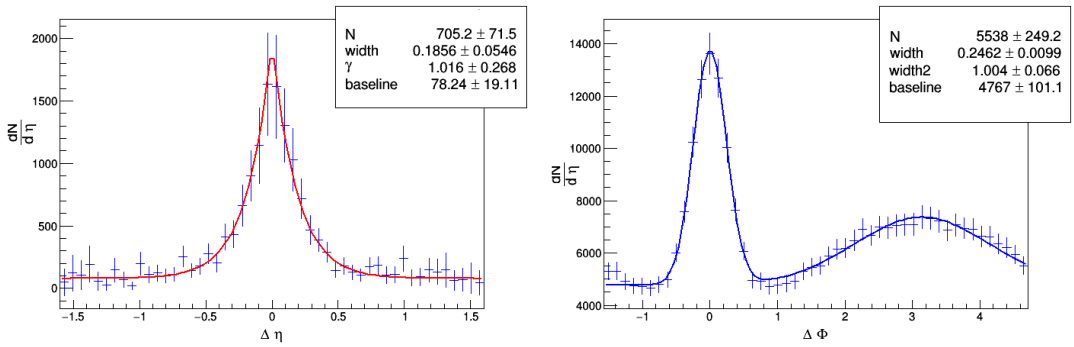

Figure 3.2: The peak in $\Delta\eta$ with near-side cut ($|\Delta\varphi| < \pi/2$) of light charged hadrons with generalised Gaussian fitting (on the **left** side) and the near-and away-side peaks of light charged hadrons in $\Delta\varphi$ plane with Gaussian fitting (on the **right** side) in PYTHIA 8 simulations.

The left panel in Figure 3.2 represents the peak in $\Delta\eta$ with near-side cut ($|\Delta\varphi| < \pi/2$) with generalised Gaussian fit. The parameter γ is unity within uncertainties, indicating a distribution that is significantly sharper than Gaussian and consistent with an exponential function. This can be understood with particle emission processes from multiple stages of the reaction, each stage having different characteristic correlation ranges. The right panel in Figure 3.2 shows the near- and away-side peaks with Gaussian fits in $\Delta\varphi$ direction. The shape of the peaks are well described by a Gaussian.

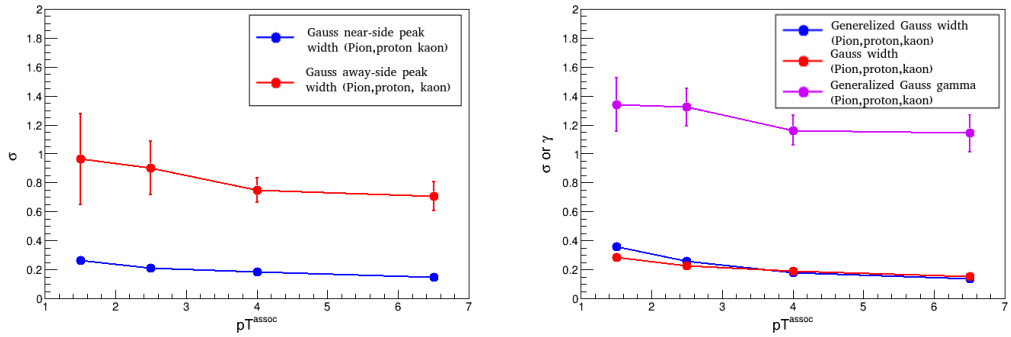

Figure 3.3: The peak width for Gaussian fitting (on the **left** side) and for generalised Gaussian fitting (on the **right** side) for $5 < p_{\mathrm{T}}^{trigger} < 8$ GeV/c and different $p_{\mathrm{T}}^{assoc.}$ values in PYTHIA 8 simulations.

To get a more comprehensive picture, I also show the fit parameters in function of p_{T}. The left panel in Figure 3.3 shows the peak width for Gaussian fitting, while the right panel in Figure 3.3

shows the peak width for generalised Gaussian fitting and the γ parameter of the function. Error bars represent the uncertainties of the fit parameters. The correlation peaks of the light charged hadrons are getting narrower towards higher p_{T}, and γ is constant within uncertainties.

3.2.2 Prompt production of heavy flavour mesons

I examined prompt production of D mesons from c quarks and B mesons from b quarks, without feed-down. In Figure 3.4 both peaks were consistent with a Gaussian. The only exception is B mesons with $5 < p_{\mathrm{T}}^{assoc.} < 8$ GeV, where the fit is significantly narrower than a Gaussian.

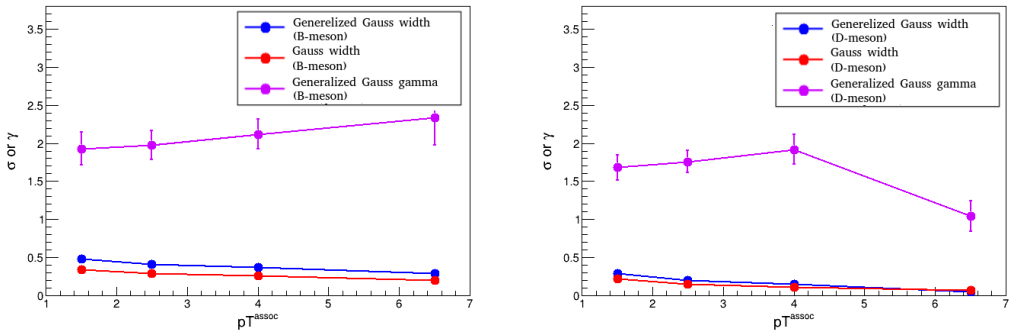

Figure 3.4: B mesons from b quarks(on the **left** side) and D mesons from c quarks (on the **right** side) and for $5 < p_{\mathrm{T}}^{trigger} < 8$ GeV/c and different p_{T}^{assoc} values in PYTHIA 8 simulations.

3.2.3 D meson from the decay of the B meson

I investigated D mesons from the decay of B mesons. The left panel in Figure 3.5 suggests a weaker dependence of both the near-side and away-side peak widths than that observed in the case of light flavor. The right panel in Figure 3.5 γ decreases with p_{T}, together with σ. (Peaks are getting both narrower and γ is less than two towards high p_{T}).

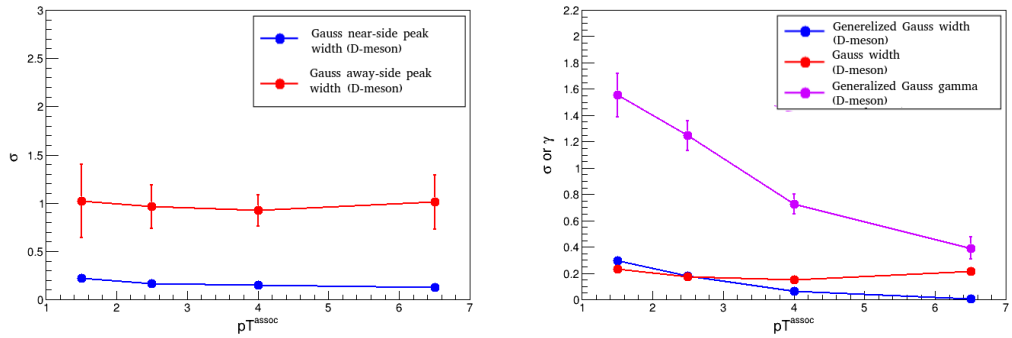

Figure 3.5: The peak width for Gaussian fitting (on the **left** side) and for generalised Gaussian fitting (on the **right** side) for D meson from the decay of the B meson for $5 < p_{\mathrm{T}}^{trigger} < 8$ GeV/c and different p_{T}^{assoc} values in PYTHIA 8 simulations.

Based on Figures 3.4 and 3.5, it is possible to distinguish between prompt D mesons and non-prompt D mesons from decays of B mesons. The statistical separation of these two contributions allows for the understanding of the flavour-dependence of heavy-quark energy loss within the

Quark-Gluon Plasma. The effect of Quark-Gluon Plasma on heavy quarks can be investigated by the ratio of D meson from b quarks and c quarks.

Feed-down D-meson contributions from beauty decays can influence the shape of the correlations. Based on the shape, Monte Carlo simulations can be used to get feed-down contribution under control. I made further investigations to understand the physics behind the D-meson and hadron correlations and how the different models describes the studied observables.

3.2.4 Investigation of electrons from B mesons

I investigated the electrons from B mesons. Electrons can come directly from semileptonic B-decays, as well as semileptonic decays of charmed mesons that B feeds down into. Still, these branching ratios are in the order of a couple of percent [38], so the electron yield is relatively low. Therefore, the lack of statistics was a limit in the analysis. However, the results are suitable for drawing conclusions.

Figure 3.6 shows that correlations of B meson decay electron with hadron produce wider correlation peaks than in the c quark decay electron case. There's no significant dependence of γ on $p_{\mathrm{T}}^{assoc.}$ and $\gamma \approx 2$.

It can be assumed that the significant deviation of the peaks from Gaussian and the strong momentum dependence of the parameters can be traced back to the decay kinematics, in which the momentum of the b quark and the location of the secondary vertex play a role. It is a well-known phenomenon that long-range correlation components from long-lived resonances lead to Lévy-like distributions rather than Gaussian [39]. It seems possible to separate the electrons coming from B mesons simply by the shape of the correlation peaks. This could be a method of identification that, combined with particle identification based on secondary vertex reconstruction in silicon tracking detectors such as the ALICE ITS [40], may provide a much better sample purity than what one can currently achieve.

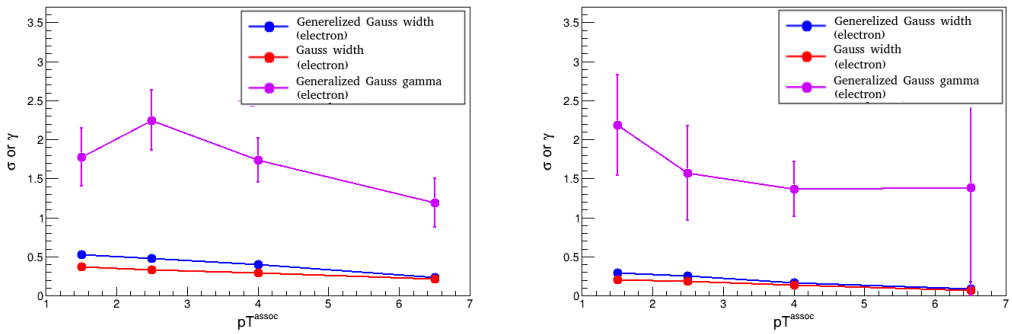

Figure 3.6: Generalised Gaussian fitting function for electrons from B mesons (**left**) and c quarks (**right**), for $5 < p_{\mathrm{T}}^{trigger} < 8$ GeV/c and different $p_{\mathrm{T}}^{assoc.}$ values in PYTHIA 8 simulations.

3.2.5 Comparison of B-meson and b-quark correlations

Finally, I compared correlations of B mesons with hadrons to b quarks with hadrons. The b quarks were taken directly from parton-level Monte Carlo truth information. In an experiment, correlations with b quarks can be constructed by taking the jet axis of b-tagged jets [41], a process that is

very problematic at low momenta, especially in heavy ion collisions. The current results show no significant difference between the two. This can be expected, as the only source of B meson is the b quark decay, besides the b quark direction is close to the axis of the b-jet, and due to its large mass the direction of the b quark momentum will determine the direction of the B meson momentum. However, higher precision is needed to verify whether the away-side peak of b quark to hadron correlations follows a similar trend to the away-side peak of B meson to hadron correlations.

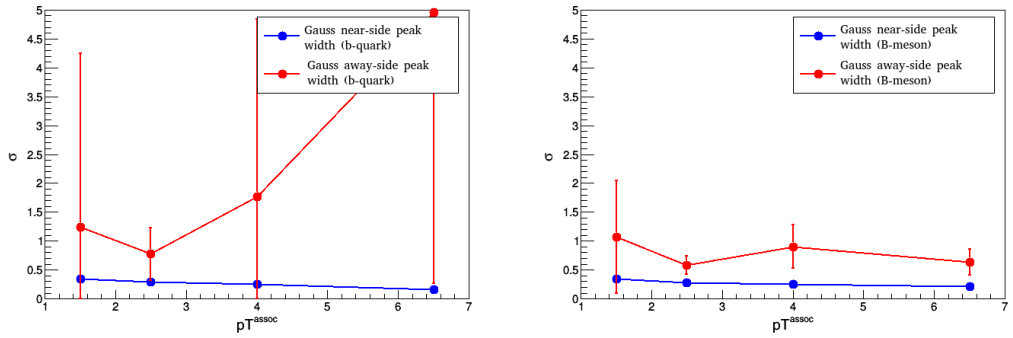

Figure 3.7: Comparsion of b quark (on the **left**) and B meson (on the **right**) correlations to hadrons in PYTHIA 8 simulations.

Figure 3.7 shows that evolution of correlation patterns with respect to transverse momentum match within uncertainties. There is a characteristic b correlation image present in both b quarks and B mesons, which is further supports that the B meson is a good proxy for the b quark.

Chapter 4

D–h correlations in ALICE

4.1 Analysis method

As a continuation of my phenomenological studies described in Chapter 3, in this chapter I describe data analysis and simulations of D meson and hadron (D–h) correlations within the ALICE experiment. I contributed to the interpretation of the ALICE results in pp and p–Pb collisions at $\sqrt{s_{\rm NN}} = 5.02$ TeV [21] with simulations within the ALICE framework [42]. Furthermore, I participate in the ongoing measurement of D–h correlations in pp collisions at $\sqrt{s} = 13$ TeV. In the followings I first summarize the ALICE analyses and then detail my results. The analyses of D–h azimuthal correlations at both $\sqrt{s_{\rm NN}} = 5.02$ and 13 TeV generally follow the methods described in Ref. [21].

4.1.1 Data samples

The data samples were collected during the 2016 LHC p–Pb run at $\sqrt{s_{\rm NN}}$ = 5.02 TeV, the 2017 LHC pp run at $\sqrt{s}$ = 5.02 TeV and 2013 LHC p–Pb run at $\sqrt{s_{\rm NN}}$ = 13 TeV. The events were selected using a minimum-bias (MB) trigger criterium matching that provided by the the V0 detector, a system of two arrays of 32 scintillators each, covering the full azimuthal angle in a pseudorapidity range of 2.8 < η < 5.1 (V0A) and -3.7 < η < -1.7 (V0C). (A minimum bias event has no specific selection criteria towards rare probes and their distributions represent inelastic collisions with as little statistical bias as possible.) The trigger condition required at least one hit in both the V0A and the V0C scintillator arrays in coincidence with the arrival of proton bunches from both directions along the beam axis. This trigger is fully efficient for recording collisions in which a D meson is produced at central rapidity.

4.1.2 Reconstruction and selection of D mesons and primary charged particles

Charmed mesons are produced in the hadronisation of charm and bottom quarks. D^0, D^+,D^{*+} and D_s^+ mesons and their antiparticles were reconstructed in the central rapidity region from their charged hadronic decay channels (4.1).

In the case of the D^0, D^+ and D_s^+ decays, the particle selection is based on the reconstruction of secondary vertex topologies. The D^{*+} meson decays at the primary vertex. D^0 candidates

Decay channel	Branching ratio
D^0 -> K^- π^+	(3.87 $\pm$ 0.05)%
D^+ -> K^- π^+ π^+	(9.13 $\pm$0.19)%
D^{*+} -> D^0 π^+	(67.7 $\pm$ 0.5)%
D_s^+ -> K^+ K^- π^+	(2.32 $\pm$ 14)%

Table 4.1: D meson's decay channels

coming from D^{*+} mesons were attached to $\pi^{\pm}$ candidate tracks at the primary vertex. The signal-to-background ratio is enhanced by applying topological selection cuts that exploit this separation between the primary and secondary vertices (the decay length). The D-mesons are defined as trigger particles, while associated particles are considered as all charged primary particles with 0.3$<$ $p_{\mathrm{T}}^{\mathrm{assoc.}}$ GeV/c and with pseudorapidity $|\eta|$ < 0.8. The charged hadron tracks were reconstructed in the ITS and TPC.

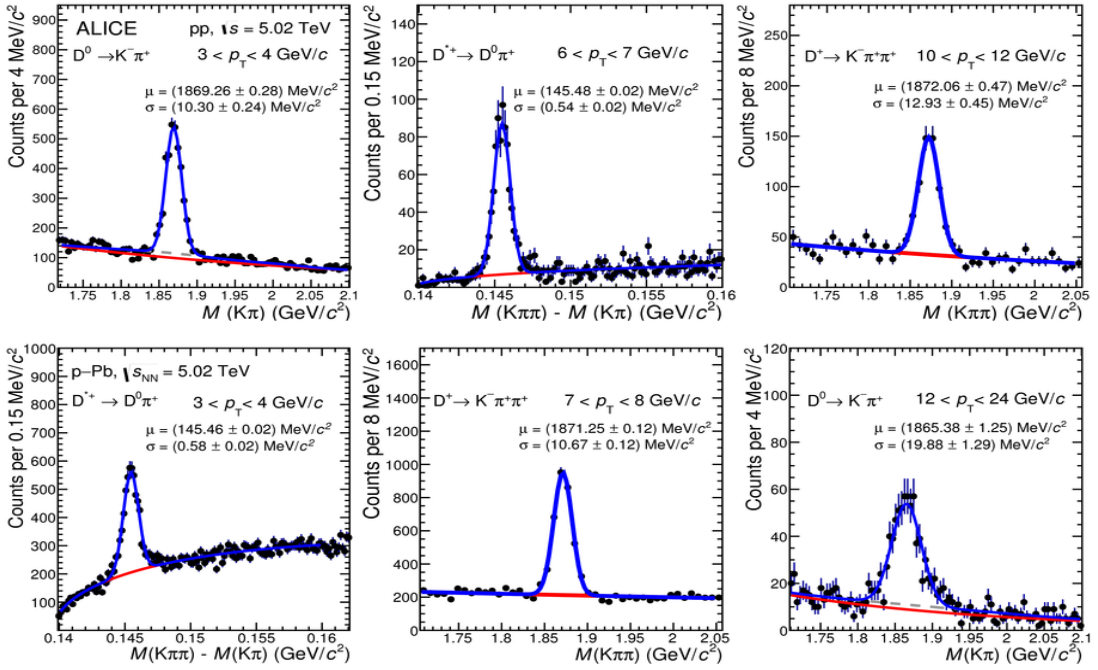

Figure 4.1: Invariant-mass (mass-difference) distributions of D^0, D^+, D^{*+} in three p_T^D intervals at $\sqrt{s}$ = 5.02 TeV for pp collisions (top row) and for p–Pb collisions (bottom row) [21].

In this analysis, average correlations of the prompt non-strange D^0, D^+ and D^{*+} mesons raw yields were extracted from fits applied to the invariant-mass (M) distributions of D^0, D^+ candidates, and to the distribution of the mass difference $\Delta M = M(K\pi\pi) - M(K\pi)$ for D^{*+} candidates. Figure 4.1 displays the invariant-mass distributions.

4.1.3 Evaluation and correction of the azimuthal-correlation distributions

D-meson candidates are selected from the range $|M - \mu| < 2\sigma$ (peak region), where M is the invariant mass, while μ and σ denote the mean and width of the Gaussian term of the invariant-

mass fit function. The correlation distribution $C(\Delta\varphi, \Delta\eta)$ was evaluated in several $p_{\mathrm{T}}^{\mathrm{D}}$ and $p_{\mathrm{T}}^{\mathrm{assoc.}}$ intervals.

Due to the limited detector acceptance and detector spatial inhomogeneities, a correction factor is obtained with the mixed event technique. In this method, data is analyzed so that D mesons from each event are paired with tracks from other events with similar z of the primary vertex and multiplicity and the correlation distributions are normalized to the values obtained at $(\Delta\varphi, \Delta\eta) = (0, 0)$.

Each D–h correlation entry is weighted by the inverse of the track reconstruction efficiency of the associated track, computed from a Monte Carlo simulation as a function of the track p_{T} and η and the z coordinate of the primary vertex. Moreover, each correlation entry is weighted by the D-meson reconstruction and selection efficiency, evaluated as a function of p_{T} and the event multiplicity from a Monte Carlo simulation.

The combinatorial background, properly normalized from the sideband region ($4\sigma < |M - \mu| < 8\sigma$), is subtracted from the peak-region correlation, as follows:

$$C(\Delta\varphi, \Delta\eta) = \frac{p_{\mathrm{prim}}(\Delta\varphi)}{S_{\mathrm{peak}}} \left(\frac{C(\Delta\varphi, \Delta\eta)}{\mathrm{ME}(\Delta\varphi, \Delta\eta)} \bigg|_{\mathrm{peak}} - \frac{B_{\mathrm{peak}}}{B_{\mathrm{sidebands}}} \frac{C(\Delta\varphi, \Delta\eta)}{\mathrm{ME}(\Delta\varphi, \Delta\eta)} \bigg|_{\mathrm{sidebands}} \right), \quad (4.1)$$

where $\mathrm{ME}(\Delta\varphi, \Delta\eta)_{\mathrm{peak}}$ and $\mathrm{ME}(\Delta\varphi, \Delta\eta)_{\mathrm{sidebands}}$ are the peak and sideband region event mixing distributions, S_{peak} provides a normalization to the number of D mesons, $p_{\mathrm{prim}}(\Delta\varphi)$ is a correction for the residual contamination of non-primary associated particles not rejected by the track selection (purity correction), B_{peak} and B_{sideband} are the amount of background triggers in the peak and in the sideband region.

The fraction of D mesons coming from B meson decays is evaluated using the reconstruction efficiencies of prompt and secondary D mesons. Monte Carlo simulations based on PYTHIA 8 are used to obtain a template of angular correlations between D mesons from B meson decays and charged hadrons, which is then subtracted from the inclusive D–h correlation distribution obtained from data.

4.1.4 Fitting method of the correlation distributions

Since the correlation distributions are symmetric around $\Delta\varphi = 0$ and $\Delta\varphi = \pi$, they were reflected in the range $0 < \Delta\varphi < \pi$ to reduce statistical fluctuations. In order to quantify the properties of the average D-meson azimuthal-correlation distribution, it was fitted with the following function:

$$f(\Delta\varphi) = b + \frac{Y_{NS} \cdot \beta}{2\alpha\Gamma(1/\beta)} \cdot e^{-(\frac{\Delta\varphi}{\alpha})^{\beta}} + \frac{Y_{AS}}{\sqrt{2\pi}\sigma_{AS}} \cdot e^{-\frac{(\Delta\varphi-\pi)^2}{2\sigma_{AS}^2}} \quad (4.2)$$

The fit function in Eq. 4.2 is composed of a constant term b describing the flat contribution below the correlation peaks, a generalised Gaussian term describing the near-side peak, and a Gaussian reproducing the away-side peak, illustrated in Figure 4.2. In the generalised Gaussian, the term Y_{NS} is a normalization factor for the near-side peak, the term α is related to the variance of the function, hence to its width, while the term β (in Chapter 3, it is denoted as γ for historical reasons) drives the shape of the peak (if β = 1, then it is an exponential function, the Gaussian

function is obtained from $\beta = 2$ and if $\beta > 2$, the shape of the peak is flattened). In the Gaussian, the term Y_{AS} is the width of the away-side peak and the term σ_{AS} is width of away-side peak.

The integrals of the functions describing the near- and away-side peaks correspond to the associated particle yields (i.e. the average number of associated particles contained in the peak), while the widths of the correlation peaks are described by the square root of the variance of their fitting terms, $\alpha\sqrt{\Gamma(3/\beta)/\Gamma(1/\beta)}\ \sigma_{\mathrm{AS}}$, for the near- and away-side, respectively. The baseline b represents the physical minimum of the $\Delta\varphi$ distribution.

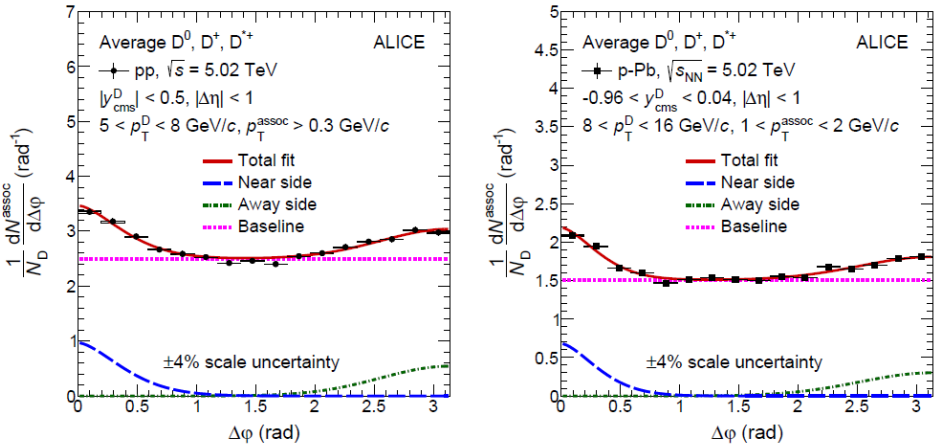

Figure 4.2: Examples of the fit to the D-meson average azimuthal-correlation distribution, for $0.3 < p_{\mathrm{T}}^{\mathrm{assoc.}} < 2$ GeV/c and $5 < p_{\mathrm{T}}^{\mathrm{D}} < 8$ GeV/c in pp collisions (left) and for $1 < p_{\mathrm{T}}^{\mathrm{assoc.}} < 2$ GeV/c and $8 < p_{\mathrm{T}}^{\mathrm{D}} < 16$ GeV/c in p–Pb collisions (right) [21].

4.2 ALICE measurements in pp and p–Pb collisions

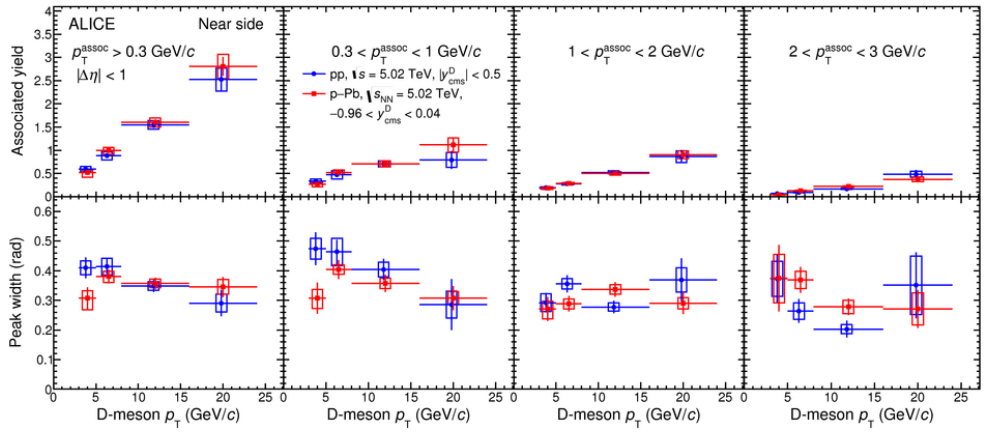

Figure 4.3: The near-side peak associated yields (first row), widths (second row) in pp and p–Pb collisions at $\sqrt{s_{\mathrm{NN}}} = 5.02$ TeV, as a function of the D-meson p_{T}, for $0.3 < p_{\mathrm{T}}^{\mathrm{assoc.}} < 1$ GeV/c, $0.3 < p_{\mathrm{T}}^{\mathrm{assoc.}} < 1$ GeV/c, $1 < p_{\mathrm{T}}^{\mathrm{assoc.}} < 2$ GeV/c, $2 < p_{\mathrm{T}}^{\mathrm{assoc.}} < 3$ GeV/c (from left to right) [21].

The measurement of the azimuthal correlation distribution of prompt D mesons with charged hadrons in pp and p–Pb collisions at $\sqrt{s_{\mathrm{NN}}} = 5.02$ TeV in the ALICE experiment were reported in Ref. [21]. The averaged D mesons with associated particles in pp and p–Pb collision systems are

compared in Figure 4.3, for four D-meson transverse momentum ranges, $3 < p_{\mathrm{T}}^{\mathrm{D}} < 5$ GeV/c, $5 < p_{\mathrm{T}}^{\mathrm{D}} < 8$ GeV/c, $8 < p_{\mathrm{T}}^{\mathrm{D}} < 16$ GeV/c and $16 < p_{\mathrm{T}}^{\mathrm{D}} < 24$ GeV/c. The distributions are presented for $0.3 < p_{\mathrm{T}}^{\mathrm{assoc.}}$ GeV/c, as well as for three sub-ranges, $0.3 < p_{\mathrm{T}}^{\mathrm{assoc.}} < 1$ GeV/c, $1 < p_{\mathrm{T}}^{\mathrm{assoc.}} < 2$ GeV/c and $2 < p_{\mathrm{T}}^{\mathrm{assoc.}} < 3$ GeV/c. In the following I examined the correlations in these ranges. In Figure 4.3 the shape of the correlation distributions and the near-side peak features are found to be compatible in pp and p–Pb collisions, showing no modifications due to nuclear effects within uncertainties. The results are qualitatively described by several LO and NLO simulations, however, there are quantitative discrepancies [21]. PYTHIA 8, which includes multiparton interactions and improved colour reconnection description, mostly describes the correlations well. For this reason I chose to perform a component level analysis with PYTHIA 8 to amend and interpret these measurements, as described in the followings.

4.3 Component-level simulations in the ALICE framework

To accomplish my analysis, I adapted my simulations to the ALICE framework [43]. The first step was performing the event generation for which I used PYTHIA 8.1. The physics components are controlled by many parameters. The simulation works with pp, $\mathrm{p\bar{p}}$, $\mathrm{e^+e^-}$ and $\mu^+\mu^-$ incoming beams. I investigated only pp collisions. As a next step I used the GEANT3 package [44], which includes a detailed description of the apparatus geometry and of the detector response. At the end of this step, realistic events are available, as they could be observed by a detector and the results are reconstructed similarly to the experimental data.

Hard QCD events were generated using 4C, Monash and MonashStar settings tuned to PYTHIA default LHC pp data. (In those cases when I do not specifically mention, which tune I used, I generated the events with 4C.) The tunes I used are detailed in Section 4.4.1. The phase space has been reduced so that the leading hard process has at least 5 GeV/c momentum. The events were selected using a minimum-bias (MB) trigger criterium matching that provided by the the V0 detector. For the simulations we required the presence of a D meson in the event, obtained by generating pp collisions containing a $\mathrm{c\bar{c}}$ or $\mathrm{b\bar{b}}$ pair in the pseudorapidity range $|\eta| < 1$.

4.4 Results at $\sqrt{s} = 5.02$ TeV

The measurement of the azimuthal correlation distribution of prompt D mesons with charged particles in pp and p–Pb collisions at $\sqrt{s_{\mathrm{NN}}} = 5.02$ TeV with the ALICE detector at the LHC was reported [21]. In order to deepen the physical understanding on the development of correlation distributions via the production, parton shower and fragmentation in heavy-flavor events, I carried out a component-level simulation analysis within the ALICE framework. These results have been accepted by the Experiment as ALICE Simulation results.

I investigated the azimuthal-correlation distributions of D mesons with associated particles, as well as the near- and away-side peak yields and widths and the β parameter of the near-side peak with predictions from PYTHIA 8 Monte Carlo event generator in pp collisions. The azimuthal-correlation distributions of the averaged D mesons with associated particles in pp collision systems are examined for four D-meson transverse momentum ranges, $3 < p_{\mathrm{T}}^{\mathrm{D}} < 5$ GeV/c, $5 < p_{\mathrm{T}}^{\mathrm{D}} < 8$

GeV/c, $8 < p_{\mathrm{T}}^{\mathrm{D}} < 16$ GeV/c, and $16 < p_{\mathrm{T}}^{\mathrm{D}} < 24$ GeV/c. The distributions are presented for $p_{\mathrm{T}}^{\mathrm{assoc.}} > 0.3$ GeV/c, as well as for three sub-ranges, $0.3 < p_{\mathrm{T}}^{\mathrm{assoc.}} < 1$ GeV/c, $1 < p_{\mathrm{T}}^{\mathrm{assoc.}} < 2$ GeV/c, and $2 < p_{\mathrm{T}}^{\mathrm{assoc.}} < 3$ GeV/c.

4.4.1 Comparison of different PYTHIA tunes

PYTHIA 8 contains several parameters that display uncertainty in our understanding of nature, in account of some physics aspects that cannot be obtained from first principles. PYTHIA parameters can be varied independently of each other, but the physical requirement of a sensible description of a set of data leads to correlations between the parameters. A given configuration of these parameters, optimized for reproducing experimental results in certain physical aspects, are called tunes.

I compared three widely used PYTHIA tunes: the 4C, the Monash and the MonashStar. The Monash tune, which uses the NNPDF2.3LO parton distribution function (PDF) set [45], is specifically configured to both $\mathrm{e^+e^-}$ and $\mathrm{pp/p\bar{p}}$ data [46]. MonashStar (or CUETP8M1-NNPDF2.3LO) is an underlying-event tune based on the Monash tune and was configured to CMS data [47]. The 4C tune is a newer one introduced with PYTHIA version 8.145 [48]. It is based on the tune 2C, but it uses the CTEQ6L1 PDF set [49] and has further changes including a reduced cross section for diffraction and modified multi-parton interaction parameters to produce a higher and more rapidly increasing charged pseudorapidity plateau for better agreement with some early key LHC numbers [50].

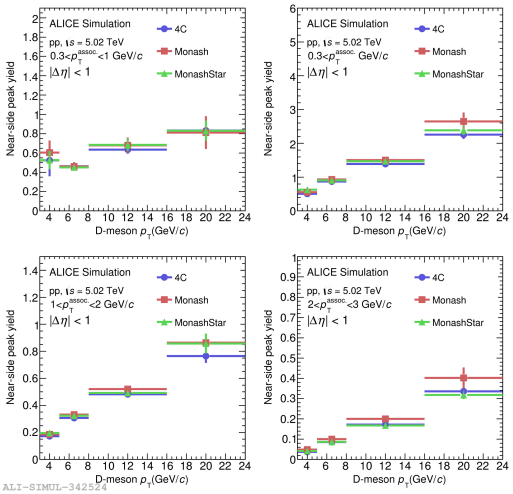

Figure 4.4: Near-side yields from fits to PYTHIA 8 simulations of D–h correlations in $\sqrt{s} = 5.02$ TeV pp collisions, as a function of D meson transverse momentum for different tunes in different $p_{\mathrm{T}}^{\mathrm{assoc.}}$ ranges.

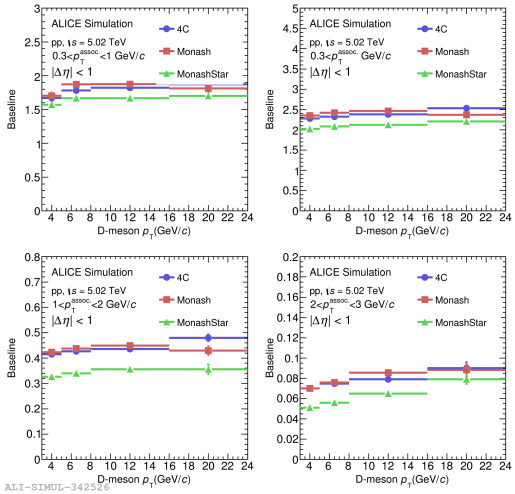

Figure 4.5: Baseline from fits to PYTHIA 8 simulations of D–h correlations in $\sqrt{s} = 5.02TeV$ pp collisions, as a function of D meson transverse momentum for different tunes in different $p_{\mathrm{T}}^{\mathrm{assoc.}}$ ranges.

Comparison of the near- and away-side peak features and p_{T} evolution can be obtained by fitting the azimuthal-correlation distributions and evaluating the peak yields and widths. Figure 4.4 and 4.5 compares these observables for the near-side correlation peaks for different tunes in pp collisions, by the PYTHIA 8 event generator as a function of the D meson p_{T}, for $p_{\mathrm{T}}^{\mathrm{assoc.}} > 0.3$

GeV/c and in three $p_{\mathrm{T}}^{\mathrm{assoc.}}$ sub-ranges.

Near side peaks are similarly predicted to Ref. [21]. The baseline is significantly lower for MonashStar (at most about 20 %), since it includes different underlying events.

4.4.2 Different colour reconnection modes

I also investigated different colour reconnection (CR) schemes provided by PYTHIA, including turning off this feature.

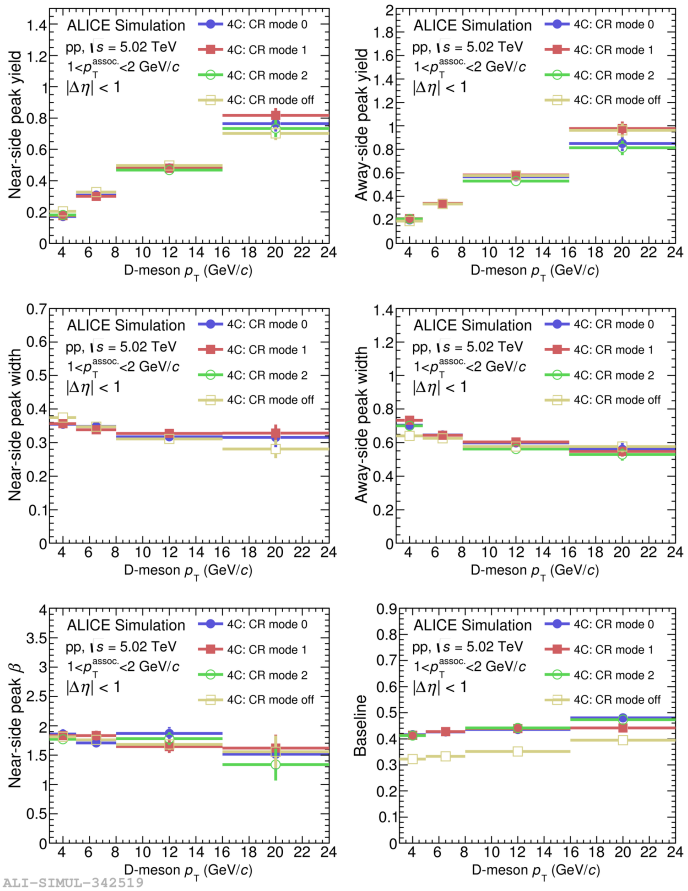

Figure 4.6: Near- and away-side peak yield (top row), width (middle row), β parameter and baseline (bottom row) of D–h correlations from simulations with different colour reconnection modes in pp collision at $\sqrt{s} = 5.02$ TeV, as a function of the D-meson p_{T}, for $1 < p_{\mathrm{T}}^{\mathrm{assoc.}} < 2$ GeV/c.

The original MPI-based scheme used in PYTHIA 8.226 (that I denote as CR mode 0 in the followings) relies on the parton shower-like configuration of the beam remnant. In an additional step, it merges the gluons of a lower-p_{T} MPI system with gluons of a higher-p_{T} MPI system. A newer QCD-based scheme [51] (CR mode 1) relies, however, on the full QCD colour configuration in the beam remnant. Then the colour reconnection is made by minimizing the potential string energy. The QCD colour rules are incorporated in the CR to determine the probability that a reconnection is allowed. This model also allows the creation of junction structures. Besides the above mentioned CR schemes, a so-called gluon move scheme [52] (CR mode 2) has been implemented to PYTHIA recently, in which gluons can be moved from one location to another so as to reduce the total string length.

Figure 4.6 compares the near- and away-side peak features and p_{T} evolution for different colour reconnection models in pp collisions, by the PYTHIA 8 event generator, for $1 < p_{\mathrm{T}}^{\mathrm{assoc.}} < 2$ GeV/c and for different $p_{\mathrm{T}}^{\mathrm{D}}$ ranges. An increasing trend of the near-side and away-side yield with increasing $p_{\mathrm{T}}^{\mathrm{D}}$ can be observed in the top row. In the middle row we can see a tendency for narrowing of the near-side and away-side peak with increasing $p_{\mathrm{T}}^{\mathrm{D}}$. In the case of the baseline the different colour reconnection modes give similar results. When we turn off the colour reconnection the baseline decreases, indicating a strong change in the underlying event by the presence of the colour reconnection. This is in agreement with the observation of other studies [53].

4.4.3 Different parton level contributions

I examined the three different parton-level contributions implemented in PYTHIA 8: multi-parton interaction (MPI), initial-state radiation (ISR) and final-state radiation (FSR).

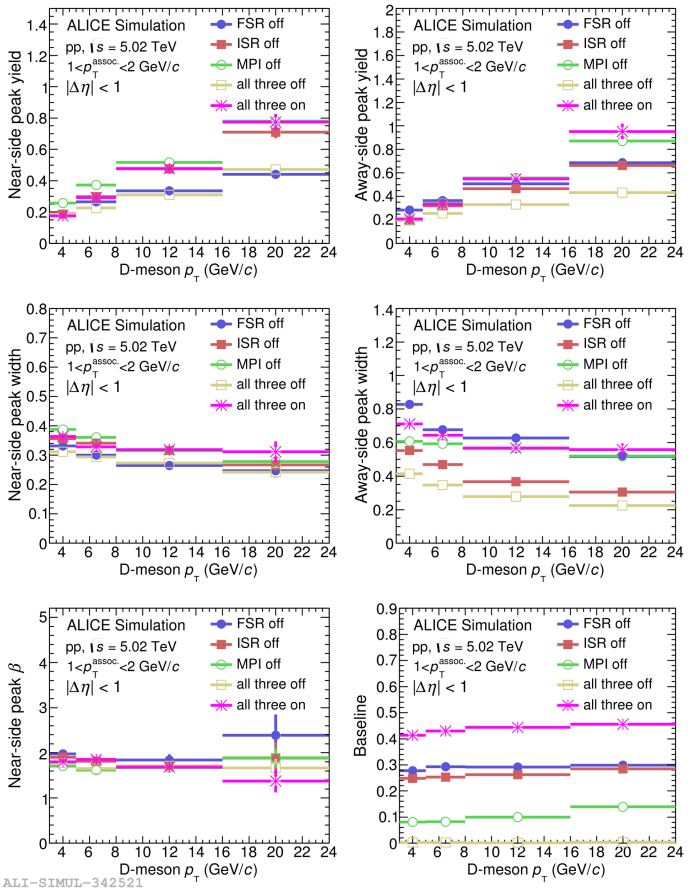

Figure 4.7: Near- and away-side peak yield (top row), width (middle row), β parameter and baseline (bottom row) of D–h correlations from simulations with different parton level contributions in pp collisions at $\sqrt{s} = 5.02$ TeV, as a function of the D-meson p_{T}, for $1 < p_{\mathrm{T}}^{\mathrm{assoc.}} < 2$ GeV/c.

Protons contain several QCD partons, so it is likely that there will be multiple parton-parton interactions (MPI) in many pp collisions at LHC energies. As detailed previously, initial and final state radiation refers to certain kinds of radiative emissions that are not due to particle annihilation. In the case of initial-state radiation, one of the incoming particles emit radiation (such as a photon) before the interaction with the others, so reduces the beam energy prior to the momentum trans-

fer, while for final-state radiation, the scattered particles emit radiation, and since the momentum transfer has already occurred, the resulting beam energy decreases.

Figure 4.7 compares the near- and away-side peak features and p_{T} evolution for different parton level contributions in pp collisions, by the PYTHIA 8 event generator, for $1 < p_{\mathrm{T}}^{\mathrm{assoc.}} < 2$ GeV/c and for different $p_{\mathrm{T}}^{\mathrm{D}}$ ranges. In the top row, the near-side yield shows significant contribution of FSR at higher $p_{\mathrm{T}}^{\mathrm{D}}$, while the away-side width demonstrates significant contribution from both FSR and ISR. In the middle row, the near-side width and shape display no change, which attests to the expectation that the shape of the near-side peak is driven by the fragmentation and the hadronic stage. As expected, the away-side peak is wider than the near-side peak because of a combined contribution of parton-level effects (with ISR having the strongest role). When FSR is turned off, it overshoots the physical case (all on). The observation that ISR does not influence the near-side peak observables, can probably be understood considering that these early parton radiations tend not to influence jet development with a given p_{T} but they may statistically shift the p_{T} class in which the paired jet falls. In the bottom row the baseline presents the contributions of parton-level effects to the underlying event as expected. Although all three effects contribute to the baseline, the most pronounced one is MPI, and the observed p_{T}-leading depenence is weak. This is expected since MPI mostly affect the underlying event, which is largely independent from the leading hard process. Figure 4.8 shows an example of the associated yield of D–h correlations from simulations with different parton level contributions.

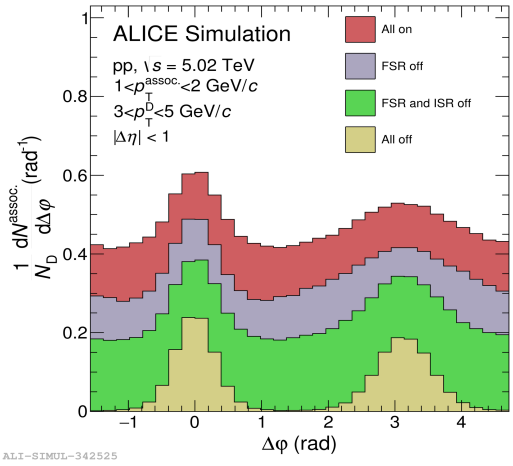

Figure 4.8: Associated yield of D–h correlations from simulations with different parton level contributions of prompt D mesons with hadrons in simulated pp collisions at $\sqrt{s} = 5.02$ TeV, for $1 < p_{\mathrm{T}}^{\mathrm{assoc.}} < 2$ GeV/c and $3 < p_{\mathrm{T}}^{\mathrm{D}} < 5$GeV/$c$.

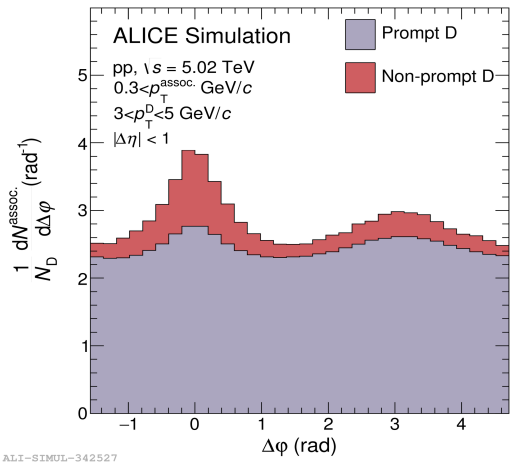

Figure 4.9: Associated yield of prompt and non-prompt D meson correlations with hadrons in simulated pp collisions at $\sqrt{s} = 5.02$ TeV, for $p_{\mathrm{T}}^{\mathrm{assoc.}} > 0.3$ GeV/c and $3 < p_{\mathrm{T}}^{\mathrm{D}} < 5$GeV/$c$.

4.4.4 Separation of prompt and non-prompt D mesons

I examined the direct decay cases of D mesons from c quarks and D mesons from the decay of B mesons. Figure 4.9 shows an example of the associated yield of prompt and non-prompt D meson correlations and Figure 4.10 shows a strong dependence of the different parameters on which particle comes from later decay. The non-prompt D meson is significantly higher for the near-side

and away-side yields (about 50% at most) and for the baseline (about 10% at most). The near-side shapes are significantly different at low $p_{\mathrm{T}}^{\mathrm{D}}$.

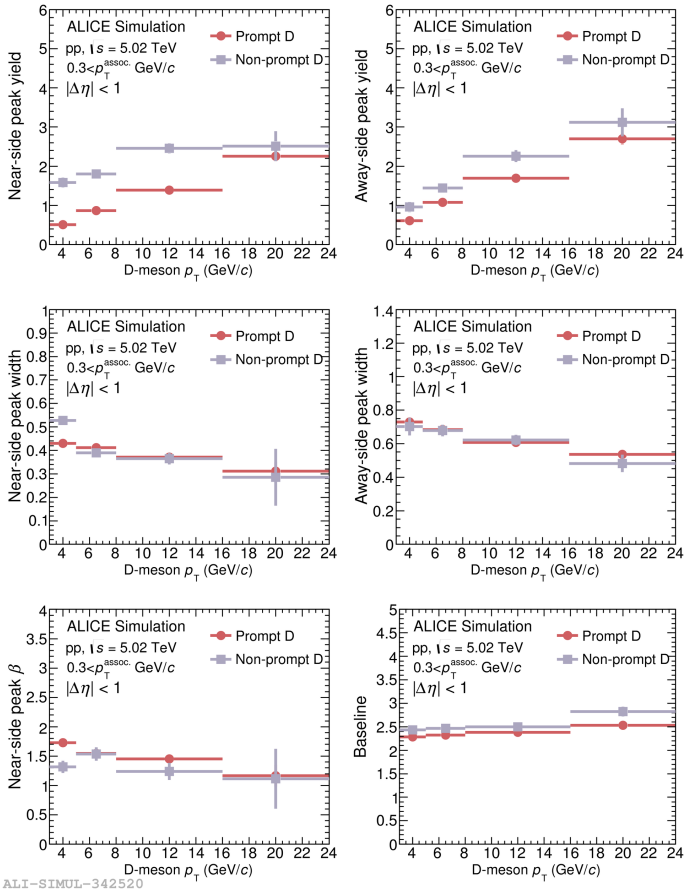

Figure 4.10: Near- and away-side peak yield (top row), width (middle row), β parameter and baseline (bottom row) of prompt and non-prompt D meson correlations with hadrons in simulated pp collisions at $\sqrt{s} = 5.02$ TeV, as a function of the D-meson p_{T}, for $p_{\mathrm{T}}^{\mathrm{assoc.}} > 0.3$ GeV/c.

It is possible to distinguish between prompt D mesons and non-prompt D mesons from decays of B mesons. The statistical separation of these two contributions in heavy-ion collisions allows for the understanding of the flavour-dependence of heavy-quark energy loss within the Quark-Gluon Plasma. Different energy loss will be manifested in altered ratios of prompt and feed-down D mesons. Therefore I could verify previous particle-level simulations using ALICE detector simulations.

4.4.5 Heavy-flavour fragmentation models

In this section, I compare two heavy-flavour fragmentation models: the Lund and the Peterson models. The Lund model is a phenomenological model of hadronization that has been used as a standard in the field since its emergence. It treats all but the highest-energy gluons as field lines, which are attracted to each other due to the gluon self-interaction and so form a narrow tube of

strong colour field. The Lund formula [54] is:

$$f(z) = \frac{(1-z)^a}{z} \exp\left(-\frac{bm_{\perp h}^2}{z}\right), \tag{4.3}$$

where $f(z)$ is the parton density in colliding hadron, z is the momentum fraction, $m_\perp = \sqrt{m^2 + p_\perp^2}$ is the transverse mass and a and b are parameters. It explains many features of hadronization quite well. In particular, the model predicts that in addition to the particle jets formed along the original paths of two separating quarks, there will be a spray of hadrons produced between the jets by the string itself—which is precisely what is observed. The Peterson formula (Eq. 4.4) is a fragmentation function for heavy quarks [55]. We can use this instead of the Lund formula, in consideration of better agreement can be obtained for fits to experimental data.

$$f(z) = \frac{1}{z(1 - \frac{1}{z} - \frac{\epsilon}{1-z})^2}, \tag{4.4}$$

where ϵ is the ratio of the effective light and heavy quark masses.

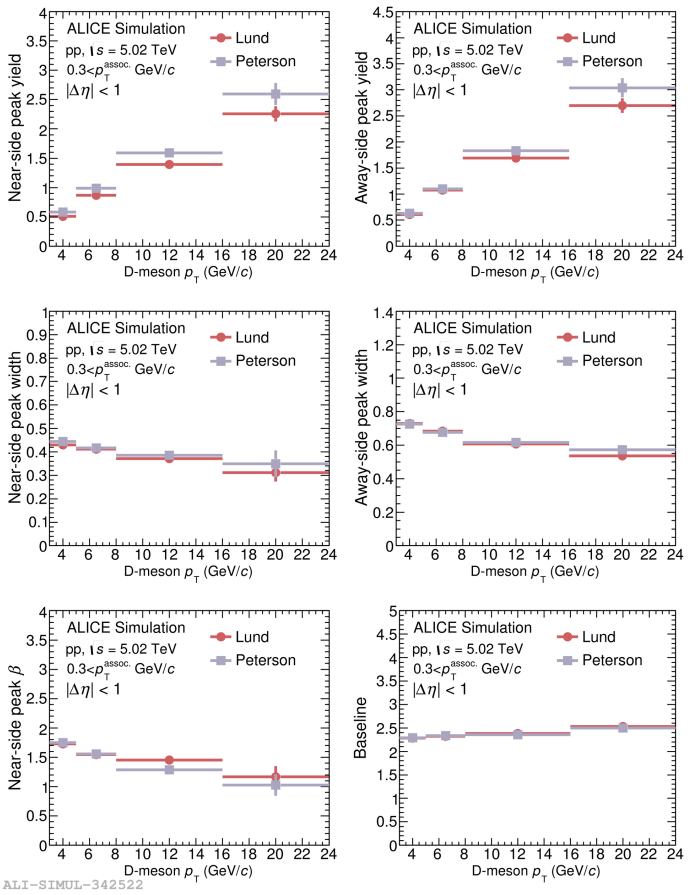

Figure 4.11: Near- and away-side peak yield (top row), width (middle row), β parameter and baseline (bottom row) of simulated D–h correlations with different heavy-flavour fragmentation models in pp collision at $\sqrt{s} = 5.02$ TeV, as a function of the D-meson p_{T}, for $p_{\mathrm{T}}^{\mathrm{assoc.}} > 0.3$ GeV/c.

Figure 4.11 compares the near- and away-side peak features and p_{T} evolution for the Lund

and the Peterson heavy-flavour fragmentation models in pp collisions, by the PYTHIA 8 event generator, for $0.3 < p_{\mathrm{T}}^{\mathrm{assoc.}}$ GeV/c and for different $p_{\mathrm{T}}^{\mathrm{D}}$ ranges. It presents hints of different trends towards higher D-meson p_{T}, but there is no significant difference between the two models.

4.4.6 The dead cone effect

A natural question is how the quark mass influences the quark evolution and its hadronic jets. When charged particles are produced in high-energy collisions, they are usually accompanied by final-state radiation (FSR). In the heavy quark case QCD predicts a suppression of soft gluon emission within a cone with a given angle around the moving direction of a charged particle. This is called the dead cone effect [56, 57, 58]. The pattern of radiation depends crucially on the mass of the emitter but not on its spin, where radiation from quarks with mass m and energy E is suppressed for emission angles $\theta \leq m/E$. We expect to see a modified fragmentation in the correlations, due to the dead cone effect.

In order to purely disentangle the dead cone effect from other differences that may show up between heavy- and light-flavour correlations, I disabled the charm quark mass. In Figure 4.12 there are slight differences at the near-side width and yield and at low $p_{\mathrm{T}}^{\mathrm{D}}$. This confirms that the differences in fragmentation of light and heavy quarks are accessible with angular correlation measurements.

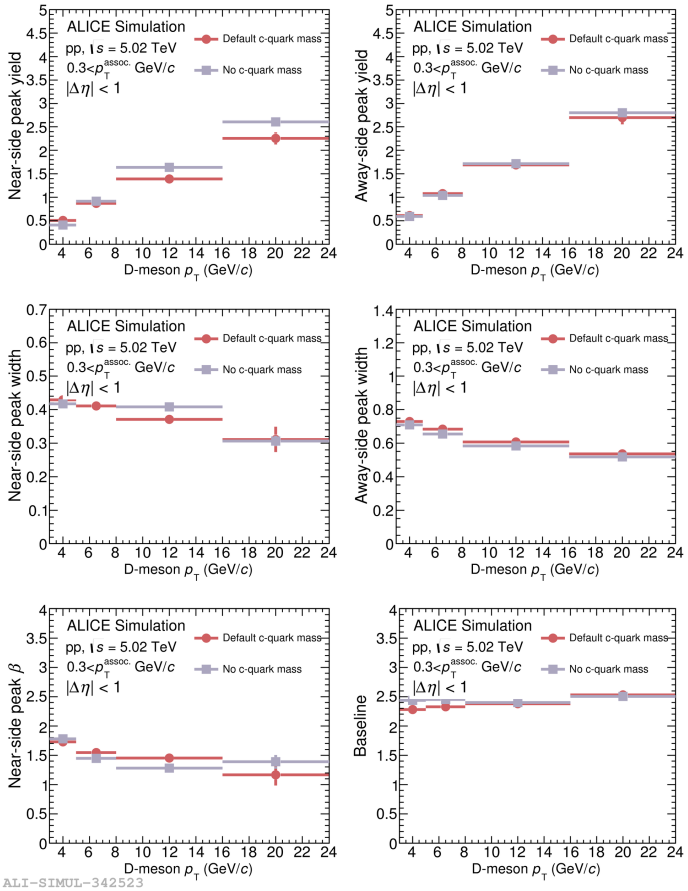

Figure 4.12: Effect of c-quark mass for the near- and away-side peak yield (top row), width (middle row), β parameter and baseline (bottom row) of simulated D–h correlations at $\sqrt{s} = 5.02$ TeV, as a function of the D-meson p_{T}, for $p_{\mathrm{T}}^{\mathrm{assoc.}} > 0.3$ GeV/c.

4.5 Results at $\sqrt{s} = 13$ TeV

In the followings I show work-in-progress azimuthal-correlation distributions of D mesons with charged particles at $\sqrt{s} = 13$ TeV in pp collisions, as well as the near- and away-side peak yields and widths and the β parameter of the near-side peak in the ALICE experiment and compare it with predictions from PYTHIA 8 Monte Carlo event generator, as well as with results from $\sqrt{s} =$ 5.02 TeV. The systematic uncertainties on ALICE correlation data are not yet final, and are not propagated to the uncertainties of the fit parameters, that therefore do not represent the complete uncertainty of the data.

4.5.1 Comparison of different PYTHIA tunes with ALICE data

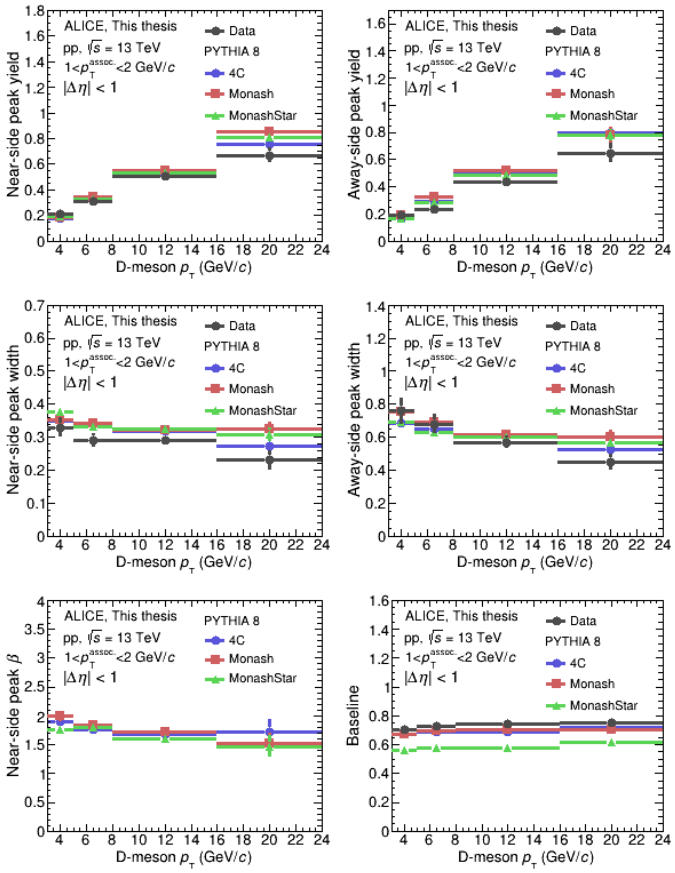

Figure 4.13: Near- and away-side peak yield (top row), width (middle row), β parameter and baseline (bottom row) of D–h correlations with different PYTHIA 8 tunes compared to ALICE data in pp collision at $\sqrt{s} = 13$ TeV, as a function of the D-meson p_{T}, for $1 < p_{\mathrm{T}}^{\mathrm{assoc.}} < 2$ GeV/c.

Figure 4.13 shows the parameters of correlation peaks for different PYTHIA 8 tunes in pp collisions, as a function of the D meson p_{T}, for $1<p_{\mathrm{T}}^{\mathrm{assoc.}} < 2$ GeV/c.

The best description is given by the 4C tune for most of the parameters. For low $p_{\mathrm{T}}^{\mathrm{D}}$, the away-side peak width is best described by the Monash tune. The baseline is significantly lower for MonashStar (~ 20 % at maximum), since it includes different underlying events. This comparison already demonstrates that correlation measurements serve as a sensitive observable to test

different, otherwise well-performing simulation tunes.

4.5.2 Dependence of the correlations on the collision energy

Angular correlation peaks are mostly sensitive to jet development and therefore little dependence is expected on the collision energy, especially at higher p_{T}. Partonic processes can, however, be different and may show up in the patterns. Current experimental data may not be precise enough to show these differences. Well-calibrated simulations, however, serve as an excellent tool for comparisons at different energies. Figure 4.14 compares the near- and away-side peak features and p_{T} evolution for different parton level contributions at $\sqrt{s}$ = 13 TeV in pp collisions, by the PYTHIA 8 event generator, for $1 < p_{\mathrm{T}}^{\mathrm{assoc.}} < 2$ GeV/c and for different $p_{\mathrm{T}}^{\mathrm{D}}$ ranges. The observations here, in general, are very similar to those obtained in the $\sqrt{s} = 5.02$ TeV results. The near-side yield, in the top row, displays significant contribution of FSR at higher $p_{\mathrm{T}}^{\mathrm{D}}$, while the away-side width indicates significant contribution from both FSR and ISR. The near-side width and shape, in the middle row, demonstrates no change, presumably, because it is driven by fragmentation/hadronic state. The away-side width is wider as expected, as a result of contributions of parton-level effects (especially ISR).

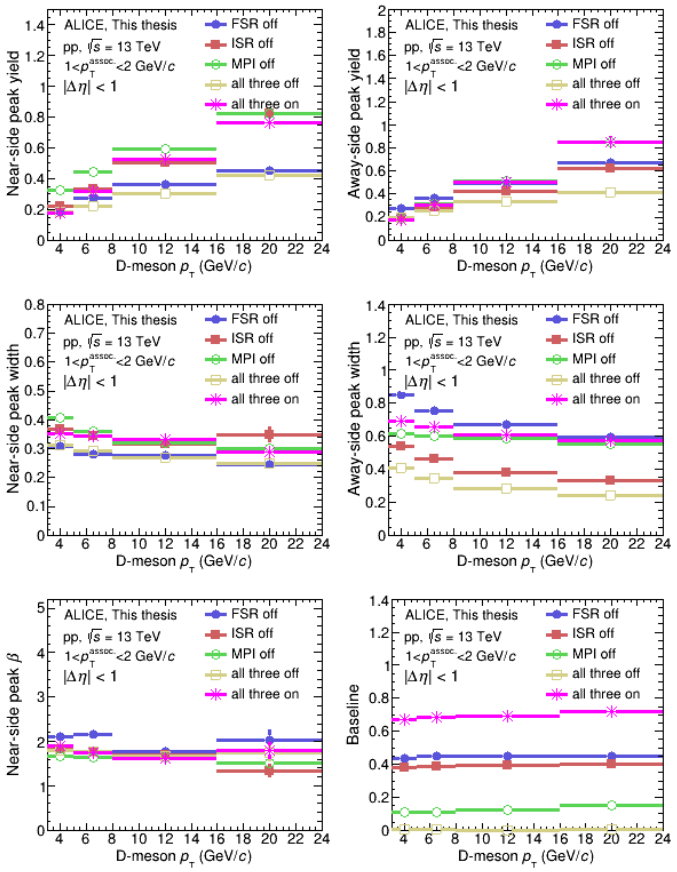

Figure 4.14: Near- and away-side peak yield (top row), width (middle row), β parameter and baseline (bottom row) of simulated D–h correlations with different parton level contributions in pp collision at $\sqrt{s} = 13$ TeV, as a function of the D-meson p_{T}, for $1 < p_{\mathrm{T}}^{\mathrm{assoc.}} < 2$ GeV/c.

A quantitative comparison can be obtained by dividing the correlation parameters from the two

energies with each other. Figure 4.15 shows the near- and away-side peak features and p_{T} evolution for different parton level contributions of $\sqrt{s} = 13$ TeV simulations divided by $\sqrt{s} = 5.02$ TeV simulations, in pp collisions, by the PYTHIA 8 event generator, for $1 < p_{\mathrm{T}}^{\mathrm{assoc.}} < 2$ GeV/c and for different $p_{\mathrm{T}}^{\mathrm{D}}$ ranges. The peak parameters are close to unity, showing that the development of heavy-flavor jets do not depend strongly on the collision energy.

The baselines are significantly higher at $\sqrt{s} = 13$ TeV than at $\sqrt{s} = 5.02$ TeV, which one can clearly see in Figures 4.16 and 4.17 compared to Figure 4.8. This difference is only present if partonic effects are turned on, and the effect mostly stems from the MPI and to the less extent from ISR and FSR. This is expected since the average UE-activity increases with collision energy through these effects, thus increasing long-range correlations. It is also remarkable that a slight but significant increase in the near-side width is observable, that is independent from parton-level processes. While the reason for this is not obvious, a possible explanation is that the generalised Gaussian width is sensitive to the tails of the distribution and thus to the soft part of the underlying event may enter show up in this parameter. This assumption can be verified with multiplicity-dependent analyses on a given energy.

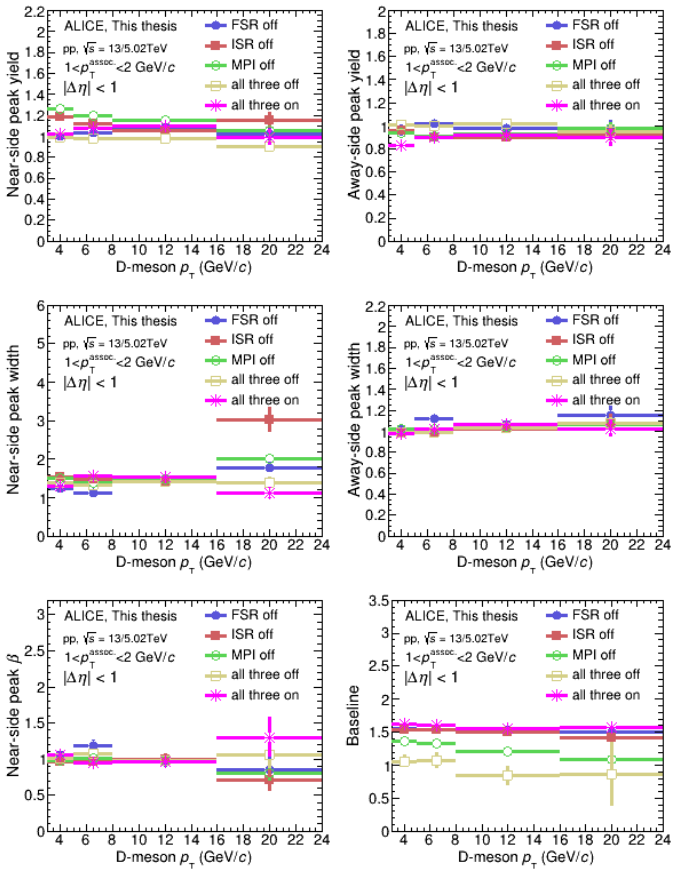

Figure 4.15: Ratios of simulation parameters at $\sqrt{s} = 13$ TeV to $\sqrt{s} = 5.02$ TeV: near- and away-side peak yield (top row), width (middle row), β parameter and baseline (bottom row) of D–h correlations with different parton level contributions in pp collision at $\sqrt{s} = 13$ TeV, as a function of the D-meson p_{T}, for $1 < p_{\mathrm{T}}^{\mathrm{assoc.}} < 2$ GeV/c.

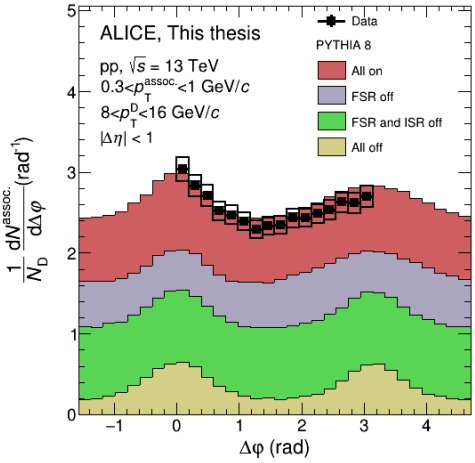

Figure 4.16: Associated yield of D–h correlations from simulations with different parton level contributions of prompt D mesons with hadrons in simulated pp collisions compared to data at $\sqrt{s} = 13$ TeV, for $0.3 < p_{\mathrm{T}}^{\mathrm{assoc.}} < 1$ GeV/c and $8 < p_{\mathrm{T}}^{\mathrm{D}} < 16$ GeV/c.

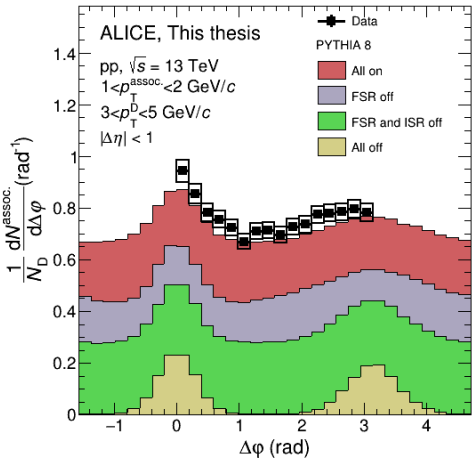

Figure 4.17: Associated yield of D–h correlations from simulations with different parton level contributions of prompt D mesons with hadrons in simulated pp collisions compared to data at $\sqrt{s} = 13$ TeV, for $1 < p_{\mathrm{T}}^{\mathrm{assoc.}} < 2$ GeV/c and $3 < p_{\mathrm{T}}^{\mathrm{D}} < 5$ GeV/c.

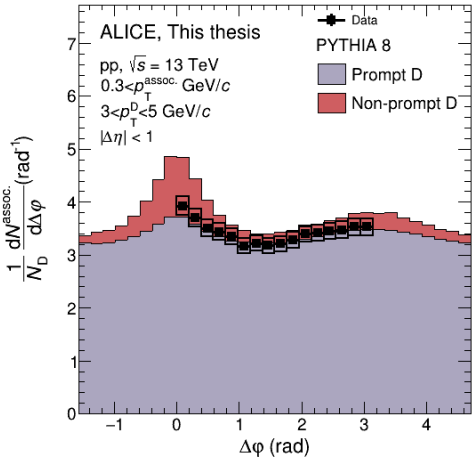

Figure 4.18: Associated yield of prompt and non-prompt D meson correlations with hadrons in simulated pp collisions compared to data at $\sqrt{s} = 13$ TeV compared to data, for $0.3 < p_{\mathrm{T}}^{\mathrm{assoc.}}$ GeV/c and $3 < p_{\mathrm{T}}^{\mathrm{D}} < 5$ GeV/c.

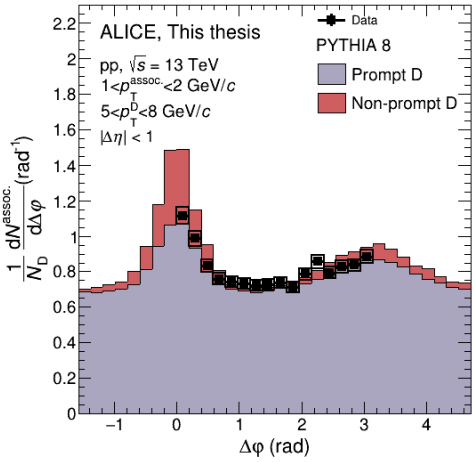

Figure 4.19: Associated yield of prompt and non-prompt D meson correlations with hadrons in simulated pp collisions compared to data at $\sqrt{s} = 13$ TeV, for $1 < p_{\mathrm{T}}^{\mathrm{assoc.}} < 2$ GeV/c and $5 < p_{\mathrm{T}}^{\mathrm{D}} < 8$ GeV/c.

Figures 4.18 and 4.19 show prompt D mesons at $\sqrt{s} = 13$ TeV compared to PYTHIA 8 simulations, as well as non-prompt D meson simulations at $\sqrt{s} = 13$ TeV. Compared to Figure 4.9, one cannot see a significant difference in the shape of the correlation peaks. The main difference, again, is that the baseline increases with increasing energy.

Chapter 5

Summary

In this thesis I summarized analyses of azimuthal-correlation distributions of D mesons and light hadrons. In a phenomenological study I have shown that a detailed analysis of heavy-flavour correlations can help in understanding flavour-dependent fragmentation as well as aid particle identification. Correlation images are sensitive to the distribution of secondary vertices of heavy-quark decays, and the latter processes can be statistically separated from light quarks. Based on a correlation picture it is possible to distinguish between prompt D mesons and non-prompt D mesons from decays of B mesons. I also suggested that this could be used as a method of identification that, combined with particle identification in secondary vertex detectors, may provide a much better sample purity than traditional methods. Furthermore, the statistical separation of these two contributions allows for the understanding of the flavour-dependence of heavy-quark energy loss within the Quark-Gluon Plasma. We also see a characteristic b-correlation image, which is present in both b quarks and B mesons. B mesons can thus be used to study b quarks in the momentum regime where the reconstruction of b jets is not feasible.

In connection to the ALICE measurements in pp and p–Pb collisions at $\sqrt{s_{NN}} = 5.02$ TeV and pp collisions at $\sqrt{s} = 13$ TeV, I carried out a component-level investigation of the correlation patterns with Monte Carlo event generators. Comparison of different PYTHIA tunes with the data highlight the importance of underlying event contribution to background. I also found that while colour reconnection has an important role in correlations, there is no significant difference between the predictions of the three examined colour reconnection models. We observe that the contribution of parton-level effects mostly affect the underlying event and away-side peak. While the away-side width is sensitive to the multi-parton interactions (MPI) contribution, the baseline is effected by the initial and final-state radiations (ISR, FSR) and MPI. There is no significant difference depending on whether the Lund or the Peterson fragmentation model is used. There are slight differences when setting the c-quark mass to zero, showing the role of dead cone effect in fragmentation. Based on a correlation picture it is possible to distinguish between prompt D mesons and non-prompt D mesons from decays of B mesons also at the detector level.

In summary, the results obtained from the analysis contributes to model development with a better understanding the interpretation of the charm-quark production processes, their fragmentation, hadronisation, as well as aid particle identification. Heavy-flavour measurements in ultra-relativistic heavy-ion collisions provide insight to flavour-dependent energy loss mechanisms as

well as the collective and thermal behaviour of the Quark-Gluon Plasma. Correlation measurements in pp collisions provide a baseline for these studies. Currently I am extending my studies towards the multiplicity-dependent data analysis of D-meson–charged hadron correlations in $\sqrt{s} = 13$ TeV pp collisions. This will help understand in detail the connection between particle production in the underlying event and the jet peak.

Acknowledgement

This thesis becomes a reality with the kind support and help of many individuals. I would like to extend my sincere thanks to all of them.

Foremost, I would like to express my sincere gratitude and thanks to my supervisor **Róbert Vértesi** for the support of my study and research, for his patience, motivation and immense knowledge. His guidance helped me in all time of research and writing of this thesis. I could not have imagined having a better supervisor and mentor for my Master study.

Besides my supervisor, I would like to thank to **Gábor Takács** for his insightful comments and **Fabio Colamaria** for provoding me valuable guidance and suggestions.

I would like to express my special gratitude to the members of the **ALICE group** who manifested their distinguished skills in their own fields as seen in their way of correction.

This thesis is supported by the Hungarian **NKFIH/OTKA K120660** and **FK131979** grant and the **Wigner Distinguished Research Group program**.

Bibliography

[1] Shuryak E.V., Quantum Chromodynamics and the Theory of Superdense Matter. *Phys. Rep.* **61**, 71 (1980).

[2] P. Gnädig, P. Hasenfratz, J. Kuti and A. Szalay, Bag Model with Pointlike Quarks and the String Limit. *11th Rencontres de Moriond: International Meeting on Storage Ring Physics*, 417 (1976).

[3] B. Andersson, G. Gustafson and C. Peterson, A Semiclassical Model for Quark Jet Fragmentation. *Z. Phys.* **C1**, 105 (1979).

[4] M. Gyulassy, P. Lévai and I. Vitev, Jet quenching in thin plasmas. *Nucl. Phys.* **A661**, 637-640 (1999).

[5] I. Arsene *et al.* [BRAHMS Collaboration], Quark gluon plasma and color glass condensate at RHIC? The Perspective from the BRAHMS experiment. *Nucl. Phys.* **A757**, 1 (2005).

[6] K. Adcox *et al.* [PHENIX Collaboration], Formation of dense partonic matter in relativistic nucleus-nucleus collisions at RHIC: Experimental evaluation by the PHENIX collaboration. *Nucl. Phys.* **A757**, 184 (2005).

[7] B. B. Back *et al.*, The PHOBOS perspective on discoveries at RHIC. *Nucl. Phys.* **A757**, 28 (2005).

[8] J. Adams et al. [STAR], Experimental and theoretical challenges in the search for the quark gluon plasma: The STAR Collaboration's critical assessment of the evidence from RHIC collisions. *Nucl. Phys.* **A757**, 102 (2005).

[9] Adams, J. *et al.* [STAR Collaboration], Evidence from d+Au measurements for final state suppression of high p_{T} hadrons in Au+Au collisions at RHIC. *Phys. Rev. Lett.* **91**, 072304 (2003).

[10] R. Pasechnik and M. Šumbera, Phenomenological Review on Quark–Gluon Plasma: Concepts vs. Observations. *Universe*, **3**, no.1, 7 (2017).

[11] Z. Fodor and S. D. Katz, Critical point of QCD at finite T and mu, lattice results for physical quark masses. *JHEP* **0404**, 050 (2004).

[12] Maire, Antonin, Phase diagram of QCD matter : Quark-Gluon Plasma. ALICE-PHO-SKE-2015-002, (2015).

[13] R. Snellings, Elliptic Flow: A Brief Review. *New J.Phys.* **13**, 055008 (2011).

[14] A. Adare *et al.* [PHENIX], Scaling properties of azimuthal anisotropy in Au+Au and Cu+Cu collisions at $\sqrt{s_{\rm NN}} = 200$GeV. *Phys. Rev. Lett.* **98**, 162301 (2007).

[15] J. Adam *et al.* [ALICE], D-meson production in p–Pb collisions at $\sqrt{s_{\rm NN}} = 5.02$ TeV and in pp collisions at $\sqrt{s} = 7$ TeV. *Phys. Rev.* **C94**, no.5, 054908 (2016).

[16] A. Andronic *et al.*, Heavy-flavour and quarkonium production in the LHC era: from proton–proton to heavy-ion collisions. *Eur. Phys. J.* **C76**, no. 3, 107 (2016).

[17] X. Dong, Y. Lee, R. Rapp, Open Heavy-Flavor Production in Heavy-Ion Collisions. *Ann. Rev. Nucl. Part. Sci.* **69**, 417 (2019).

[18] S. Acharya *et al.* [ALICE], Production of muons from heavy-flavour hadron decays in pp collisions at $\sqrt{s}$ = 5.02 TeV. *JHEP* **09**, 008 (2019).

[19] S. Acharya *et al.* [ALICE], Measurement of D-meson production at mid-rapidity in pp collisions at $\sqrt{s} = 7$ TeV. *Eur. Phys. J.* **C77**, no.8, 550 (2017).

[20] E. Frajna and R. Vértesi, Correlation of Heavy and Light Flavors in Simulations. *Universe* **5**, no. 5, 118 (2019).

[21] S. Acharya *et al.* [ALICE Collaboration], Azimuthal correlations of prompt D mesons with charged particles in pp and p–Pb collisions at $\sqrt{s_{\rm NN}}$ = 5.02 TeV. *Preprint:* arXiv:1910.14403 [nucl-ex], (2019).

[22] Sjostrand, T., Mrenna, S., Skands, P.Z., A Brief Introduction to PYTHIA 8.1. *Comput. Phys. Commun.* **178**, 852–867 (2008).

[23] S. Chatrchyan *et al.* [CMS], Observation of Long-Range Near-Side Angular Correlations in Proton-Lead Collisions at the LHC. *Phys. Lett.* **B718**, 795-814 (2013).

[24] B. Abelev *et al.* [ALICE], Long-range angular correlations on the near and away side in p-Pb collisions at $\sqrt{s_{\rm NN}} = 5.02$ TeV. *Phys. Lett.* **B719**, 29-41 (2013).

[25] Abelev B. B. *et al.* [ALICE Collaboration], *Phys. Lett.* **B726**, 164–177, (Preprint1307.3237), (2013).

[26] M. Azarkin, P. Kotko, A. Siodmok and M. Strikman, Studying minijets and MPI with rapidity correlations. *Eur. Phys. J.* **C79**, no.3, 180 (2019).

[27] S. Schlichting and P. Tribedy, Collectivity in Small Collision Systems: An Initial-State Perspective. *Adv. High Energy Phys.* **2016**, 8460349 (2016).

[28] F. Carminati *et al.*, ALICE: Physics performance report, volume I. *J. Phys.* **G30**, 1517 (2004).

[29] B. Alessandro *et al.*, ALICE: Physics performance report, volume II. *J. Phys.* **G32**, 1295 (2006).

[30] I. Bird *et al.*, LHC computing Grid. Technical design report, CERN-LHCC-2005-024.

[31] K. Aamodt *et al.* [ALICE Collaboration], The ALICE experiment at the CERN LHC. *JINST* **3**, S08002 (2008).

[32] Adam, J. *et al.* [ALICE Collaboration], Anomalous evolution of the near-side jet peak shape in Pb-Pb collisionscat $\sqrt{s_{\rm NN}}$ = 2.76 TeV. *Phys. Rev. Lett.* **119**, 102301 (2017).

[33] A. A. Affolder *et al.*, [CDF Collaboration], Charged jet evolution and the underlying event in proton-antiproton collisions at 1.8 TeV. *Phys. Rev.* **D65**, 092002 (2002).

[34] P. Bartalini *et al.*, Multi-Parton Interactions at the LHC. Preprint: arXiv:1111.0469 [hep-ph] (2011).

[35] T. Sjöstrand, The Development of MPI Modeling in Pythia. *Adv. Ser. Direct. High Energy Phys.* **29**, 191-225 (2018).

[36] Skands, P., Carrazza, S., Rojo, J., Tuning PYTHIA 8.1: The Monash 2013 Tune. *Eur. Phys. J.* **C74**, 3024 (2014).

[37] Adamczyk, L. *et al.* [STAR Collaboration], Υ production in U + U collisions at $\sqrt{s_{\rm NN}}$ = 193 GeV measured with the STAR experiment. *Phys. Rev.* **C6**, 064904 (2016).

[38] Tanabashi, M. *et al.* [Particle Data Group], Review of Particle Physics. *Phys. Rev.* **D98**, 030001 (2018).

[39] Vértesi, R. [PHENIX Collaboration], THERMINATOR simulations and PHENIX images of a heavy tail of particle emission in 200-GeV Au+Au collisions. In *Proceedings of the 23rd Winter Workshop on Nuclear Dynamics, Big Sky, Montana, USA, 11–18 February 2007*; Bauer, W., Bellwied, R., Harris, J.W., Eds.; EP Systema: Budapest, Hungary, (2007).

[40] Yang, P., Aglieri, G., Cavicchioli, C., Chalmet, P.L., Chanlek, N., Collu, A., Gao, C., Hillemanns, H., Huang, G., Junique, A., *et al.* MAPS development for the ALICE ITS upgrade. *J. Instrum.* **10**, C03030 (2015).

[41] Jung, K. [CMS Collaboration], Measurements of b-jet Nuclear Modification Factors in pPb and PbPb Collisions with CMS. *Nucl. Phys.* **A931**, 470–474 (2014).

[42] E. Frajna, D-meson and hadron correlations in the ALICE experiment and in simulations. *19th Zimányi School Winter Workshop on heavy ion physics*, https://indi.to/tHf8p.

[43] J. F. Grosse-Oetringhaus *et al.* [ALICE], The ALICE online-offline framework for the extraction of conditions data, *J. Phys. Conf. Ser.* **219**, 022010 (2010).

[44] R. Brun, F. Bruyant, F. Carminati, S. Giani, M. Maire, A. McPherson, G. Patrick, and L. Urban, GEANT: Detector Description and Simulation Tool. (1994).

[45] R. D. Ball *et al.* [NNPDF Collaboration], Parton distributions with QED corrections. *Nucl. Phys.* **B877**, 290 (2013).

[46] P. Skands, S. Carrazza and J. Rojo, Tuning PYTHIA 8.1: the Monash 2013 Tune. *Eur. Phys. J.* **C74**, no. 8, 3024 (2014).

[47] V. Khachatryan *et al.* [CMS Collaboration], Event generator tunes obtained from underlying event and multiparton scattering measurements. *Eur. Phys. J.* **C76**, no. 3, 155 (2016).

[48] R. Corke and T. Sjöstrand, Interleaved Parton Showers and Tuning Prospects. *JHEP* **1103**, 032 (2011).

[49] J. Pumplin, D. R. Stump, J. Huston, H. L. Lai, P. M. Nadolsky and W. K. Tung, *JHEP* **0207**, 012 (2002).

[50] A. Buckley *et al.*, General-purpose event generators for LHC physics. *Phys. Rept.* **504**, 145 (2011).

[51] J. R. Christiansen and P. Z. Skands, String Formation Beyond Leading Colour. *JHEP* **1508**, 003 (2015).

[52] S. Argyropoulos and T. Sjöstrand, Effects of color reconnection on $t\bar{t}$ final states at the LHC. *JHEP* **1411**, 043 (2014).

[53] A. Ortiz and L. Valencia Palomo, Probing color reconnection with underlying event observables at the LHC energies. *Phys. Rev.* **D99**, no. 3, 034027 (2019).

[54] B. Andersson, The Lund String Model, *Cambridge University Press* (1998).

[55] C. Peterson, D. Schlatter, I. Schmitt and P. M. Zerwas, Scaling Violations in Inclusive e+ e- Annihilation Spectra. *Phys. Rev.* **D27**, 105 (1983).

[56] Yuri L. Dokshitzer, Valery A. Khoze, and S. I. Troian, Particle spectra in light and heavy quark jets. *J. Phys.* **G17**, 1481 (1991).

[57] Yuri L. Dokshitzer, Valery A. Khoze, and S. I. Troian, On specific QCD properties of heavy quark fragmentation ('dead cone'). *J. Phys.* **G17**, 1602 (1991).

[58] R. Keith Ellis, W. James Stirling, and B. R. Webber, QCD and collider physics. *Camb. Monogr. Part. Phys. Nucl. Phys. Cosmol.* **8**, 1 (1996).